Measurements of Bottom Quark-Antiquark Azimuthal Production Correlations in Proton-Antiproton Collisions at $\sqrt{s} = 1.8$ TeV

Kevin Lannon, Tony Affolder

(Dated: March 19, 2004)

We report on two different measurements of $b\bar{b}$ azimuthal angular production correlations in $p\bar{p}$ collisions at $\sqrt{s}$=1.8 TeV. The data set utilized in these measurements were taken by the Collider Detector at Fermilab using 90 pb^{-1} of data collected during 1994-1995. One technique measures the $\Delta\phi$ between bottom quarks in events with two reconstructed secondary vertex tags. The sample composition is measured as a function of $\Delta\phi$ using the two vertex tags' signed L_{xy}. The other technique uses events in which $b \to J/\psi X; \bar{b} \to \ell X'$ where ℓ is an electron or muon identified with soft lepton algorithms. The $b\bar{b}$ purity is determined as a function of $\Delta\phi$ by fitting the decay length of the J/ψ and the impact parameter of the soft lepton. Both techniques measure the fraction of the $b\bar{b}$ pairs producted in the same azimuthal hemisphere (f_{toward}). For both techniques, the measured f_{toward} values are consistent with both leading-log and next-to-leading order QCD predictions.

PACS numbers: 13.85.-t,12.38.Qk,14.65.Fy
Keywords: QCD, heavy quark production

I. INTRODUCTION

The dominant b quark production mechanism at the Tevatron is believed to be pair production through the strong interaction. However, predictions from perturbative QCD [1] have so far failed to describe the observed b single quark production cross section [2–8]. Past differential azimuthal cross section measurements [9–12] have been systematically higher than theoretical prediction, but all azimuthal shapes have been constant with theory. Possible explanations for this disagreement involve supersymmetric production mechanisms [13], improved b fragmentation models [14], and non-perterbatuve $b\bar{b}$ production mechanisms [15]. Additional measurements related to $b\bar{b}$ production are needed to determine whether experimental measurements are consistent with the Standard Model picture of $b\bar{b}$ production or with any of the proposed alternative models.

Correlations between the b quarks give information about the interactions that produce $b\bar{b}$ pairs. For example, the lowest-order QCD $b\bar{b}$ production diagrams contain only the b and $\bar{b}$ quarks in the final state. Momentum conservation requires that these quarks be produced back-to-back in azimuthal opening angle, $\Delta\phi$, and with balanced momentum transverse to the beam direction, p_T. However, when higher-order QCD processes are considered, the presence of additional light quarks and gluons in the final state allows the $\Delta\phi$ distribution to become more spread out and the b transverse momenta to become more asymmetric. Studying $b\bar{b}$ correlations gives insight into the effective contributions from higher-order QCD processes to b quark production at the Tevatron. In addition, if the measured correlations cannot be accommodated by QCD production mechanism, it would suggest a non-Standard Model source of b quarks.

QCD diagrams for $b\bar{b}$ production can be divided into three categories:

Flavor Creation consists of the lowest-order, two-to-two QCD $b\bar{b}$ production diagrams. This process includes $b\bar{b}$ production through $q\bar{q}$ annihilation and gluon fusion, plus higher-order corrections to these processes. Because this production is dominated by two-body final states, it tends to yield $b\bar{b}$ pairs that are back-to-back in $\Delta\phi$ and balanced in p_T.

Flavor Excitation refers to diagrams in which a $b\bar{b}$ pair from the quark sea of the proton or antiproton is excited into the final state because on of the quarks from the $b\bar{b}$ pair undergoes a hard QCD interaction with a parton from the other beam particle. Because only one of the quarks in the $b\bar{b}$ pair undergoes the hard scatter, this production mechanism tends to produce b quarks with asymmetric p_T. Often, one of the b quarks will be produced with high rapidity, and not be detected in the central region of the detector.

Gluon Splitting occurs when the $b\bar{b}$ pair arises from a $g \to b\bar{b}$ splitting in the initial or final state. Neither of the quarks from the $b\bar{b}$ pair participate in the hard QCD scatter. Depending on the experimental range of b quark p_T sensitivity, gluon splitting production can yield a $b\bar{b}$ distribution with a peak at small $\Delta\phi$.

Figure 1 illustrates some lowest-order examples of each type of diagram. The general trend is that flavor creation diagrams, being dominated by two-body $b\bar{b}$ final states tend to produce back-to-back $b\bar{b}$ pairs balanced in p_T, while flavor excitation and gluon splitting, which necessarily involve multiparticle final states including a $b\bar{b}$ pair and light quarks or gluons, produce $b\bar{b}$ pairs that are more smeared out in $\Delta\phi$ and p_T asymmetry. Categorizing $b\bar{b}$ diagrams in this scheme becomes ambiguous at higher orders. In addition, at higher-orders, diagrams from these three categories interfere, making a rigorous experimental decomposition of $b\bar{b}$ production into these three components technically impossible. Nonetheless, the categories provide a useful tool for understand $b\bar{b}$ on an intuitive level.

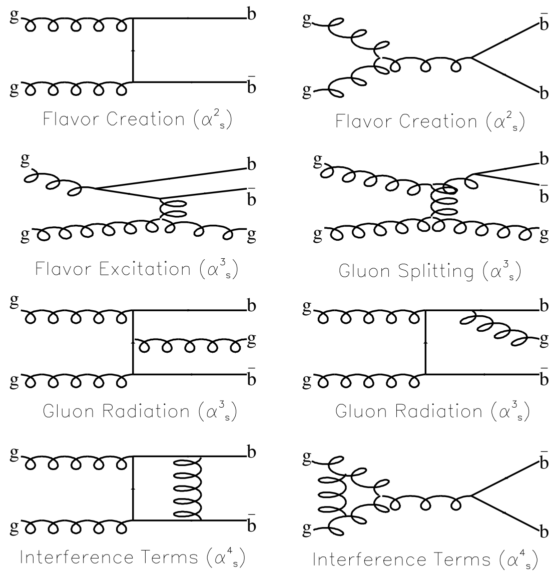

FIG. 1: Example Feynman diagrams which contribute to NLO bottom production theory predictions.

The NLO QCD calculation of $b\bar{b}$ production includes diagrams from each production mechanism up to $\mathcal{O}(\alpha_S^3)$. The NLO calculation is the lowest order approach that returns sensible results because the flavor excitation and gluon splitting diagrams–which first appear at $\mathcal{O}(\alpha_S^3)$–provide contributions on approximately the same level as the lowest-order flavor creation diagrams, which are $\mathcal{O}(\alpha_S^2)$. This can be understood by considering the cross section for $gg \to gg$ which is approximately two orders of magnitude larger than the cross section for $gg \to b\bar{b}$. Flavor excitation and gluon splitting diagrams can be formed by adding a $g \to b\bar{b}$ splitting either in the initial or final states of the $gg \to gg$ process, but even after accounting for the $\mathcal{O}(\alpha_S)$ suppression, flavor excitation and gluon splitting still provide contributions that are numerically comparable to the leading-order terms. Therefore, higher-order corrections to $b\bar{b}$ production cannot be ignored.

It is not clear a-priori that corrections beyond leading order do not psemi-leptonicaly an important role in $b\bar{b}$ production. An aalternative approach semi-leptonically estimating the effects of higher-order corrections is the parton shower model implemented by the Pythia [16, 17] and Herwig [18] Monte Carlo programs. The parton shower approach is not exact to any order in α_S but rather tries to approximate corrections to all orders by using leading-order matrix elements for the hard two-to-two QCD scatter and adding addition initial- and final-state radiation using a probabilistic approach. In this approximation, flavor creation, flavor excitation, and gluon splitting processes can be separated exactly based on how many b quarks participate in the hard, two-to-two scatter. In flavor creation events, both b quarks are part of the hard scatter. For flavor excitation, only one b quark participates in the hard scatter. In gluon splitting, neither of the b quarks participates in the hard scatter. For flavor excitation and gluon splitting, b quarks that are not a part of the hard scatter are generated as part of the initial-state or final-state showers. Interferences among the three production mechanisms are neglected as a higher-order effect in this approximation. Ref. [19] shows that parton shower Monte Carlo programs are able to better reproduce the observed b production cross section, but only if sizeable contributions from flavor excitation and gluon splitting are included. Studying $b\bar{b}$ correlations provides as way to tell whether such large contributions from these higher-order processes is supported by the data.

There have been several previous hadron collider measurements of $b\bar{b}$ correlations. UA1 [9], D0 [10], and CDF [12] have all investigated the $b\bar{b}$ $\Delta\phi$ distribution using events in which both of the B hadrons decayed to muons. In addition, CDF has measured correlations between muons from B decays and b-tagged jets [11]. In each of these analyses, the conclusion was that although the normalization between the data and theoretical predictions did not always agree, the shapes of the distributions agreed reasonably well. However, in order to reduce backgrounds, each analysis listed above introduces either a minimum invariant mass cut on the dimuon pair or a minimum angle requirement between the muon and the tagged b jet. These cuts limit the sensitivity in these analyses to $b\bar{b}$ production at small opening angles, which is where flavor excitation and gluon splitting production dominate over flavor creation. The region in which there is a small opening angle between the b quarks is interesting to study for trying to understand the significance of higher-order $b\bar{b}$ production mechanisms at hadron colliders.

In this paper, we present two new CDF measurements of the $\Delta\phi$ spectrum in $b\bar{b}$ production in $p\bar{p}$ collisions at $\sqrt{s} = 1.8$TeV. These measurements are made using approximately 90pb^{-1} of data collected during the 1994-1995 Tevatron run, known as Run 1b. The focus of these two analyses is making a measurement of the small opening angle portion of the $b\bar{b}$ $\Delta\phi$ spectrum. One analysis begins with a sample of events containing an 8 GeV electron or muon to enhance to b quark content of the sample by taking advantage of the relatively high semileptonic B branching ratio. These events are then searched for the presence of displaced secondary vertices indicating the decay of a long lived B hadron, using a vertexing algorithm similar to the SECVTX algorithm used for the top quark search [ref]. This analysis requires that the decay vertices for both B hadrons in the event be reconstructed and extracts the B hadron $\Delta\phi$ distribution from the $\Delta\phi$ distribution measured between the reconstructed secondary vertices. This technique yields a high-statistics sample of double-tagged $b\bar{b}$ events and retains sensitivity to $b\bar{b}$ pairs with small opening angles. The other analysis detects the presence of B decays in the data entirely through leptonic signatures. The decay of one B is tagged by reconstructing the decay of a $J/\psi \rightarrow \mu\mu$, which provides the trigger signature that defines this samples. Furthermore, events are required to contain an electron or muon consistent with the semileptonic decay of the other B. This approach does not yield as many double-tagged events as the first, but it retains the highest sensitivity for $b\bar{b}$ production at small opening angles and has fewer backgrounds. Both analyses produce consistent results indicating that roughly one third of the $b\bar{b}$ pairs produced in the momentum and rapidity range to which these analyses are sensitive have $\Delta\phi < 90°$. In addition, both analyses are at least qualitatively consistent with the contribution from higher-order $b\bar{b}$ predicted by Pythia and Herwig, further supporting the significance of the flavor excitation and gluon splitting production mechanisms at the Tevatron. Specific details for both of these analyses are given below.

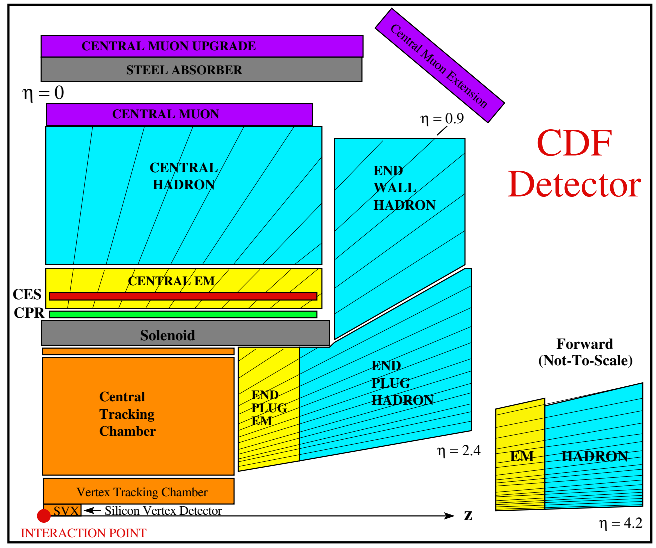

FIG. 2: Schematic of a quarter cross-section of the CDF Run 1b detector.

II. DETECTOR

The analyses described here make use of the $90pb^{-1}$ of data collected by the CDF detector during the 1994-1995 run of the Tevatron. The CDF detector possesses a cylindrical symmetry about the beam axis, making it convenient to use a cylindrical coordinate system with the z axis oriented along the beam direction, r the distance from the beam axis, and ϕ the azimuthal angle measured from the x direction, which points radially outward in the plane of the Tevatron accelerator ring. At times, it is also useful to use the polar angle θ as measured from the beam axis, or more commonly η defined as $\eta = -ln(tan(\theta/2))$. In the approximation of massless particles, η reduces to the rapidity, y, the invariant boost of the particle along the z direction. The CDF detector is described in detail elsewhere [20]. In the following, we focus on the elements most relevant for these analyses.

The tracking systems at CDF are immersed in a 1.4 T magnetic field to allow measurement of charged particle momentum in the plane transverse to the beam direction (p_T). Reconstruction of a charged particle track begins with measurements made in the central tracking chamber (CTC) [21], a large, multi-wire drift chamber containing 84 layers of wires from a radius of 31 cm to 133 cm. The layers are arranged in alternating groups of 12 wires parallel to the beam direction (known as an axial super-layer) and 6 wires with a ±3 degree stereo angle (stereo super-layer). Inside the radius of the CTC, the vertex detector (VTX) is a time projection chamber that provides a precision measurement of the charged particle trajectory in the $r - z$ direction, allowing a determination of the location of the primary interaction point along the z direction. The innermost tracking system at CDF is the silicon vertex detector (SVX') [22]. This four-layer detector covering from 2.9 cm to 8.1 cm in radius allows very high precision determination of charged particle trajectories in the $r - \phi$ plane. Combined, the CDF tracking systems provide a p_T resolution of $\delta p_T/p_T = [(0.0009\dot{p}_T)^2 + (0.0066)^2)]^{1/2}$ and an impact parameter resolution of $\delta d_0 = [13 + (40GeV/c)/p_T]\mu m$.

Electron identification is provided by the central electro-magnetic calorimeter (CEM) [23] located just outside the radius of the CTC. The CEM consists of alternating layers of lead absorber and polystyrene scintillator. The CEM is designed to be deep enough to contain electro-magnetic showers initiated by electrons and photons. A set of wire and strip tracking chambers (known as the CES chambers) are located at the shower maximum depth, or depth of greatest energy deposition, to measure the transverse profile of the shower. For more penetrating particles, the central hadronic calorimeter (CHA) [24] is located behind the CEM. Like the CEM, the CHA is constructed from alternating layers of steel absorber and scintillator. An electron is identified using a track reconstructed in the CDF tracking systems that points to an energy deposit in the CEM of appropriate size. The CHA is used in this analysis primarily to veto hadrons that might otherwise mimic an electron signature. At CDF, muons are detected by their ability to penetrate the material in the calorimeter. Two sets of muon chambers are used to identify muons. The first set, known as the central muon system (CMU) [25] is located just outside the radius of the CHA (3.47 m). To reach the CMU, a particle produced at the primary vertex perpendicular to the beam direction must traverse 5.4 pion interaction lengths of material. An additional set of chambers known as the central muon upgrade (CMP) [26] are arranged in a rectangular array around the central detector behind an additional 60 cm of steel shielding to provide further discriminating power between real muons and hadronic punch-through. To penetrate to the CMP, a particle traveling perpendicular to the beam direction from the primary interaction passes through 8.4 pion interaction lengths of material. Together, the CMU and CMP detectors provide muon coverage over the pseudo-rapidity range $|\eta| < 0.6$. Additional pseudo-rapidity coverage is provided by the central muon extension chambers (CMX) which cover $0.6 < \eta < 1.0$. The CMX consists of four arches of drift chambers located behind 6.2 interaction lengths of material. In addition the CMX drift tubes are sandwiched between two layers of scintillator that provide fast timing information to the trigger.

CDF uses a three level trigger system. The first two levels are implemented in hardware and are capable of reducing the data rate from the full 300 kHz beam crossing rate to a more manageable 20 Hz. The third trigger level consists of software reconstruction algorithms that run a stream-lined version of the full CDF reconstruction software. The triggers used for this analysis rely on lepton identification through matching energy deposition the CEM (for electrons) or muon hits the the CMU, CMP, and CMX (for muons) with charge particle tracks reconstructed in the CTC.

III. SECONDARY VERTEX TAG CORRELATION ANALYSIS

A. Overview

The main motivation of this analysis is to explore the region of production in which the b and $\bar{b}$ quarks have a small opening angle. To this end, we begin by collecting a large sample of B decays from $90pb^{-1}$ of data taken at CDF during the 1994-1995 Tevatron run. To create a sample enhanced in b quark content, we demand that the events contain a lepton, either electron or muon, with $p_T > 8GeV/c$. In addition, we use a vertex tagging algorithm similar to the SECVTX algorithm [XX] mentioned above, to tag the displaced decay vertices of both B hadrons in the event. The b-tagging algorithm used for this analysis has been specially optimized from previous versions to enable tagging of B hadron pairs with arbitrarily small opening angle. After background removal, we obtain a sample of approximately 17,000 double-tagged $b\bar{b}$ events, the largest sample ever collected at a hadron collider. Using the sample above, we measure the $\Delta\phi$ distribution between the reconstructed secondary vertex tag pairs and predictions based on PYTHIA and HERWIG Monte Carlo programs. In addition, we use information from the Monte Carlo samples to correct the tag-pair $\Delta\phi$ for detector effects and backgrounds to allow an extraction of the B hadron $\Delta\phi$ distribution that can be directly compared to theoretical predictions from other models. We choose to measure the B hadron $\Delta\phi$ distribution rather than the $b\bar{b}$ distribution because our secondary vertex tags are more directly related to B hadrons than b quarks. Converting our measurement from the B hadron level to the b quark level would introduce a dependence on b quark fragmentation models that we wish to avoid.

B. Sample Selection

This analysis starts with the same basic data sample used for the measurement of time dependent B mixing at CDF [27]. This sample, characterized by the presence of at least one electron or muon with $p_T > 8GeV/c$ plus at least one reconstructed secondary decay vertex, is known as the BVTX sample because the algorithm used to reconstruct, or tag, secondary vertices is known as the BVTX algorithm. The BVTX algorithm is based on the SECVTX b-tagging algorithm used for the Run 1 top analysis [ref]. For more information on the BVTX algorithm, consult refs [ref]and [ref]. The original BVTX sample used for the B mixing analysis consists of over 480,000 electron-triggered events and over 430,000 muon-triggered events.

Our basic event selection strategy is as follows: We start with the events from the BVTX sample, which is a loosely selected sample of events containing at least one electron or muon with $p_T > 8GeV/c$, identified using standard CDF lepton identification cuts [ref] and at least one secondary vertex. We impose stricter cuts on the trigger lepton to ensure all B hadron decays producing the trigger lepton are kinematically similar. Next, we reprocess the data using a modified version of the BVTX tagging algorithm (see Section XX below) and demand that each selected event contain at least two secondary vertex tags. The separation between each secondary vertex and the primary vertex in the plane perpendicular to the beam (L_{xy}), divided by the uncertainty on the separation is required to be at least two. In addition, the 2-D separation between the secondary vertex pairs is required to satisfy $|\Delta L_{xy}|/\sigma_{\Delta L_{xy}}$ to reduce the chance of tagging the same B decay with two poorly measured tags. Each tag pair is required to have an invariant mass greater than $6GeV/c^2$ that a tag pair results from a $B \to D \to X$ decay chain. For a pair of tags failing either the $|\Delta L_{xy}|/\sigma_{\Delta L_{xy}}$ or the invariant mass cuts, only the tag with the longest 2-D separation from the primary vertex is removed. Finally, since the trigger requirements for this sample assume at least one of the B hadrons decay semi-leptonically, the trigger lepton is required to be within a cone of $\Delta R = \sqrt{\Delta\phi^2 + \Delta\eta^2} = 1.0$ of one of the vertices.

C. Secondary Vertex Tagging

The secondary vertex finding algorithm is based on the BVTX algorithm used for the B mixing analysis [27] which is itself a modified version of the SECVTX algorithm used for the CDF top quark analysis [ref]. This algorithm uses precision tracking information from the

CDF tracking system to identify tracks consistent with coming from a secondary vertex significantly displaced from the primary interaction vertex. The main difference between the version of the BVTX algorithm used here and the version used for previous CDF analysis is the ability of the algorithm to locate more than one secondary vertex per jet searched. For extensive details on the BVTX algorithm and the modifications made for this analysis, see ref [ref]. Below we summarize the secondary vertex finding approach.

Secondary vertex finding begins by first locating the primary interaction vertex for the event using precision tracking information from the SVX' and VTX. Next the tracks in the event passing quality cuts are grouped into jets using a cone-based clustering algorithm with a cone size of $\Delta R = 1.0$. Each jet is then searched for the presence of one or more secondary vertices displaced from the primary. The secondary vertex finding is done in two passes for each jet. The first pass finds secondary vertices containing at least three tracks. When the first pass fails to find any more secondary vertices in a jet, a second pass is attempted in which the individual track cuts are made more stringent and two-track secondary vertices are accepted. Each secondary vertex found is required to be significantly displaced from the primary and not to be consistent with the decay of a K_S^0 or Λ.

D. Sample Composition

The purpose of identifying a sample of lepton events containing two or more secondary vertex tags is to isolate a high purity sample of $b\bar{b}$ events. However, there are other sources of double-tagged events that contribute to this sample. Table XX lists the various contributions. Briefly, we treat each contribution below.

A mistag occurs when the vertex finding algorithm fits a vertex from a set of tracks that dont physically originate from a common decay vertex. It is occasionally possible because of measurement errors or random chance to find a set of prompt tracks that seem to intersect at a vertex separated from the primary. Also, when b quarks are produced with a small opening angle, it is not hard to combine tracks from two different B hadron decays, sometimes with additional prompt tracks, accidentally to form a false vertex that doesnt correspond to the decay point of either B. These decay vertices distort the spectrum of correlations and must be removed in order to get a good quality measurement. One way to identify mistags is by looking at the signed L_{xy} distribution. L_{xy} is signed based on the inferred direction of the particle that decayed to produce the secondary vertex tag relative to the primary vertex. A particle that seems to be moving out from the primary vertex at the time of decay is given a positive L_{xy}, while a particle that seems to have been moving towards the primary vertex when it decayed is assigned a negative L_{xy}. In principal, a secondary vertex tag corresponding to the decay of real, long-lived particle will have a positive L_{xy} although the finite resolution of the secondary vertex algorithm can yield a negative contribution. Mistags have an L_{xy} distribution that is symmetric about zero. One can use this feature of mistags to subtract them statistically from the data in a similar fashion to subtracting the appropriately normalized distribution from the side-bands of a mass peak to remove the background contribution. For single tag distributions, if we plot the distribution for all tags having Lxy ¡ 0, to a good approximation, we will have the distribution for mistags only. The distribution for Lxy ¿ 0 is a mixture of the distribution for good tags and the distribution for mistags. For single-tag distributions, we can remove the mistag component by subtracting twice the distribution for tags with negative L_{xy} from the distribution for all tags. The formula for distributions involving tag pairs is more complicated and is given in equation XX below:

$$N_{GG} = N_{++} - N_{+-} - N_{--} + N_{--} \tag{1}$$

where N_{GG} is the estimated number of tag pairs in which both tags are legitimate secondary vertex tags while, N_{++} is the number of tag pairs in which both tags have L_{xy}, N_{+-} and N_{-+} are the number of tag pairs in which one tag has positive L_{xy} and one has negative L_{xy}, and N_{--} is the number of tags pairs in which both tags have $L_{xy} < 0$.

Another possible source of background involves tagging more than one secondary vertex from a single B decay. These tags, known as sequential tags, are most likely to occur when the B decay involves the production of a D hadron that travels a certain distance from the B decay vertex before itself decaying. The invariant mass cut of $6GeV/c^2$ eliminates virtually all contribution from this source. It is also possible that some sequential tag pairs arise from tracking errors that cause tracks actually originating from a common vertex to be reconstructed as coming from two vertices that are very close together. The cut on the significance of the two-dimensional separation between the tags ($|\Delta L_{xy}|/\sigma_{\Delta L_{xy}}$) eliminates nearly all these tag pairs. The residual contribution from sequential double tags is estimated in Section XX.

Finally, a background source of legitimate secondary decay vertices is $c\bar{c}$ production. In general, most D hadrons have a much smaller lifetime than B hadrons. However, those D hadrons that do live long enough to produce a secondary vertex capable of being tagged by BVTX will not be removed or accounted for by any of the methods mentioned above. In addition, it is HERWIG-possible to have events in which multiple heavy flavor pairs, such as $b\bar{b}+c\bar{c}$ are produced. For example, in a flavor creation event, an additional $c\bar{c}$ pair may be produced through gluon splitting. In such events it is possible for the $b\bar{b}$ to contribute one tag and the $c\bar{c}$ pair to contribute another. Although the rate of multiple heavy flavor production is much lower than single $b\bar{b}$ pair production, the opportunity to tag more displaced vertices in a given event can provide an enhancement in tagging efficiency, meaning such processes cannot be discounted outright. Studies indicate that the contribution to the double tag sample from prompt charm and multiple heavy flavor production is not large, roughly 10

E. Monte Carlo Samples

For this analysis, the parton shower Monte Carlo programs PYTHIA and HERWIG are used to generate large samples of events from $b\overline{b}$ production. Because flavor creation, flavor excitation, and gluon splitting do not interfere with one another in the leading-log approximation, each production mechanisms is generated separately for maximum efficiency. For PYTHIA, the flavor creation sample was generated using the heavy flavor production process (MSEL = 5) which uses massive matrix elements for $q\overline{q} \rightarrow b\overline{b}$ and $gg \rightarrow b\overline{b}$ diagrams. Flavor excitation and gluon splitting were produced with the generic QCD two-to-two process (MSEL = 1), which uses massless matrix elements. Flavor excitation and gluon splitting events are separated from other QCD processes by examining the partons that participate in the two-to-two hard scatter. Three separate PYTHIA samples are generated, each with a different amount of initial state radiation, as controlled by the parameter $PARP(67)$. For all three PYTHIA samples, the underlying event is tuned to match observations in CDF data [ref]. On the other hand, because there are fewer parameters to tune, only a single HERWIG sample is generated. The flavor creation and flavor excitation components of the sample are made using HERWIG heavy flavor production option (IPROC = 1705) which include massive matrix element treatments of the leading order flavor creation and flavor excitation diagrams. As in PYTHIA, HERWIGs gluon splitting component results from generation all QCD two-to-two processes (IPROC = 1500) using massless matrix elements and retaining those events classified as gluon splitting based on the partons involved in the hard scatter. In addition, a small sample of $c\overline{c}$ events was generated using PYTHIA, for the purposes of evaluating the possible effects of residual prompt charm as a background for this analysis. For both samples, details of the D and B decays are handled by the CLEO QQ Monte Carlo program. Finally, to make the Monte Carlo data resembled the actual data as closely as possible, the Monte Carlo events are passed through a fast CDF detector simulation, a CDF trigger simulation, and the same reconstruction and analysis code used for the actual data. Additional details regarding the generation of Monte Carlo samples for this analysis can be found in ref [ref].

F. Data–Monte Carlo Comparison

After the Monte Carlo samples have been passed through the detector simulation as described above, the Monte Carlo predictions for the secondary vertex tag distributions can be compared directly with data. Distributions involving only individual tags have more or less the same shape for flavor creation, flavor excitation, and gluon splitting, and so these distributions can be used to check whether the detector simulation adequately models the real detectors effect on the data. Distributions involving tag pairs, and therefore correlations, give information about how well the Monte Carlo models describe $b\overline{b}$ production.

Figure XX shows the comparison of the trigger lepton transverse momentum between the data and each Monte Carlo sample. Figure XX shows the comparison of the secondary vertex tag momentum in the Monte Carlo and data. In each case, the agreement between the measured spectrum from the data and the predicted spectra for each Monte Carlo sample indicates that the effects of trigger and reconstruction thresholds are adequately modeled in the simulation. In addition, examining the Monte Carlo truth information for the B hadrons tagged by the analysis code allows a determination of the effective minimum Bp_T sensitivity for this analysis. For the B producing the 8 GeV/c trigger lepton, the minimum p_T is 14 GeV/c, while the other B must have at least 7.5 GeV/c p_T in order to be tagged by the BVTX algorithm.

Comparing tag pair correlations between the Monte Carlo samples and the data reveals whether PYTHIA or HERWIG provide an adequate model of the higher-order contributions to $b\overline{b}$ production. This analysis focuses on the transverse opening angle, $\Delta\phi$. For tag pairs, $\Delta\phi$ is defined as the angle between the p_T vectors determined by taking the vector sum of the p_T from all the tracks involved in the tag. The $\Delta\phi$ distribution is interesting to study because it is sensitive to contributions from flavor excitation and gluon splitting. Also, the broadness of the back-to-back peak in $\Delta\phi$ is sensitive to the amount of initial-state radiation present in the Monte Carlo. It should be noted that the shape of the $\Delta\phi$ distribution and the relative contributions from the three production mechanisms depend on the p_T cuts placed each of the B hadrons.

There are two possible approaches to normalizing the relative contributions in Monte Carlo from flavor creation, flavor excitation, and gluon splitting. PYTHIA and HERWIG each provide predictions for the cross section of each production mechanism, and these cross sections can be used to normalize their contributions relative to one another. Alternatively, one could take the position that PYTHIA and HERWIG may not correctly model the amount of each contribution, and the relative contributions should be determined to provide the best match to data. In this analysis, both approaches will be examined. As described in the sections below, the data is compared to the Monte Carlo predictions in two ways. First, the Monte Carlo prediction for the cross section of each production mechanism is used to normalize the flavor excitation and gluon splitting components relative to the flavor creation contribution. In this fixed normalization scheme, the data is compared to the Monte Carlo using one arbitrary global normalization parameter. The arbitrary global normalization is included because this analysis attempts only a shape comparison, not an absolute cross section measurement. In addition, the Monte Carlo and data are compared using a floating normalization scheme. In this comparison, each production mechanism is given an independent arbitrary normalization constant and the three normalizations are varied to yield the best match to data.

Figure XX shows the comparison of the BVTX tag $\Delta\phi$ distribution from data to the distribution predicted by each Monte Carlo sample when the relative normalizations of each production mechanism is based on the Monte Carlo prediction for the cross sections of the different production mechanisms. From these $\Delta\phi$ comparisons it can be seen that each Monte Carlo model matches the qualitative features of the data, although there are definite differences in shape, as reflected by the poor χ^2 values. For the PYTHIA sample with low initial-state radiation (ISR) (PARP(67) = 1.0), the peak in the back-to-back region is too narrow, while for the higher ISR samples (PARP(67) = 3.0 or 4.0), the back-to-back peak is too broad. Similarly, the HERWIG Monte Carlo sample also has a peak that is too broad at high $\Delta\phi$, perhaps even more so than in PYTHIA. However, aside from these discrepancies at high $\Delta\phi$, the rest of the $\Delta\phi$ distribution matches reasonably well between Monte Carlo and data using the normalizations predicted by the Monte Carlo generators for the different production mechanisms. The χ^2 values between the $\Delta\phi$ curves from Monte Carlo and data are listed in Table XX. On the basis of these χ^2 values, it appears that PYTHIA with PARP(67) = 3.0 provides the best match to data when using the Monte Carlos default normalization for the three production mechanisms. Figure XX shows the breakdown of the contributions from the individual production mechanisms to the overall $\Delta\phi$ shape for this PYTHIA sample.

However, since, in the parton shower approximation, the contributions from flavor creation, flavor excitation, and gluon splitting may be generated separately, each component can have a separate, arbitrary normalization and the three components can be fit for the combination of normalizations that gives the best match to the shape of the $\Delta\phi$ spectrum from data. These fits are shown in Figure XX. Surprisingly, when the normalizations of the individual components are allowed to float with respect to one another, one can obtain rather good agreement in shape between data and both the lower ISR and higher ISR PYTHIA samples. The fit of the lower ISR PYTHIA Monte Carlo to the data increases the broader contribution from flavor excitation to compensate for the narrowness of the back-to-back peak from flavor creation. For the higher ISR PYTHIA samples, the peak at high $\Delta\phi$ is made narrower to match the data by all but eliminating the contribution from flavor excitation. A comparison of the relative fractions of each production mechanism in the two PYTHIA fits is shown in Figure XX. The fit of the HERWIG sample to the data also tries to compensate for the excessive broadness of the HERWIG flavor creation peak at high $\Delta\phi$, but even after completely eliminating the flavor excitation contribution, the remaining contribution from flavor creation at high $\Delta\phi$ is too broad to model the data. Table XX compares the fit quality and effective contribution from flavor creation, flavor excitation, and gluon splitting in the fits of the various Monte Carlo samples to the data. That both low ISR and high ISR PYTHIA samples can be made to fit the data with approximately the same fit quality is unexpected, especially since the low ISR sample accomplishes this fit with a high flavor excitation content while the high ISR sample fits with almost no flavor excitation contribution. In the end, there seems to be an ambiguity in PYTHIA that allows a trade-off between initial state-radiation and the amount of flavor excitation.

In general, any of the Monte Carlo samples compared to the data shows reasonable qualitative agreement. The Monte Carlo sample that best matches the data is PYTHIA with PARP(67) = 3.0 or 4.0 (higher ISR), when the individual normalizations of the flavor creation, flavor excitation, and gluon splitting are allowed to float separately to best fit the data. Although the fit using PYTHIA with PARP(67) = 1.0 is not so poor as to rule this model out completely, studies indicate that PYTHIA with higher initial state radiation does a better job of matching both the underlying event and minimum bias data at CDF [ref]. Therefore, we select the PYTHIA sample, with PARP(67) = 4.0 and the relative normalizations of flavor creation, flavor excitation, and gluon splitting fixed by our fit to the $\Delta\phi$ distribution of the data, as the best Monte Carlo model of the data. Comparisons indicate that the differences between PYTHIA with PARP(67) = 4.0 and PARP(67) = 3.0 are minor. Figure XX shows a comparison of other correlations between the data and PYTHIA with PARP(67) = 4.0.

It is interesting to note that before allowing the normalizations of each production mechanism to float in the fits, the agreement between HERWIG and the data is no worse than the agreement between the low ISR PYTHIA sample and the data. However, because the disparity between the data and the low ISR PYTHIA sample comes from the narrowness in the flavor creation peak at high $\Delta\phi$, when the normalizations are allowed to float, the fit can alleviate the disagreement by increasing the peak width through a higher contribution from flavor excitation. In contrast, for HERWIG, once the contribution from flavor excitation has been reduced to zero, the fit has no way to make the width of the back-to-back flavor creation peak smaller, short of the unphysical situation of setting the flavor excitation normalization negative. If there were some other parameter for HERWIG, like PYTHIAs initial state radiation parameter, PARP(67), that could be used to tune the width of the back-to-back flavor creation peak, it may be possible to achieve good agreement between HERWIG and the data as well.

G. Corrections and Systematics

The correlations examined so far in the data involve pairs of BVTX tags, rather than pairs of B hadrons. There are detector effects, such as the tagging efficiency for pairs of B hadrons as a function of $\Delta\phi$, that distort the shape of the measured tag pair correlations from the true B hadron distribution. In addition, residual contributions from background can affect the shape of the tag pair distribution. For the comparison between Monte Carlo and data, the detector effects are accounted for by using a detector and trigger simulation to adjust the Monte Carlo to match the conditions in the data, while the backgrounds are assumed to be negligible. However, since the Monte Carlo models examined in Section XX match the data reasonably well, Monte Carlo events can be used to determine the relationship between the measured tag pair distribution and the actual B hadron distribution. In the sections below, two kinds of corrections to the tag pair $\Delta\phi$ distribution are considered: a correction for the relative tagging efficiency, which is a detector effect, and a correction for the contributions from mistags, prompt charm, and sequentials that remain in the data after the steps taken in Section XX to remove backgrounds. In addition, the Monte Carlo is used to estimate the systematic uncertainties associated with correcting for the relative tagging efficiency and removing background events. These corrections and systematic errors are evaluated using several different Monte Carlo samples to account for uncertainties involved in the Monte Carlo model itself.

The BVTX tagging algorithm is not equally effective for all topologies of $b\bar{b}$ production. In particular, as the opening angle between the two B hadrons decreases, the BVTX algorithm has a more difficult time of reconstructing both displaced secondary vertices. This effect becomes especially severe when the two B hadrons are both contained within the cone of a single jet for track clustering purposes. Furthermore, correlations between opening angle and B p_T for the various production mechanisms can lead to differences in the relative efficiency for reconstructing tag pairs at different opening angles. These effects distort the shape of the $\Delta\phi$ distribution measured for tags from the true BB $\Delta\phi$ distribution.

We correct for these relative efficiency effects using the Monte Carlo that best matches the data, as determined in Section XX. Because we are only examining the shape of the $\Delta\phi$ distribution, our goal in making this correction is only to account for differences in the relative efficiency of the tagging algorithm, as a function of $\Delta\phi$. We do not attempt to correct for effects that impact all parts of the $\Delta\phi$ spectrum equally. For example, an overall shift in the muon trigger efficiency would not affect this correction. To determine the correction for each bin we take the ratio of the number of tag-pairs reconstructed in the Monte Carlo to the number of pairs that could have been reconstructed if the tagging algorithm had perfect efficiency. The number of tag pairs that would have been reconstructed assuming perfect efficiency is determined by looking at the generator level B hadron $\Delta\phi$ distribution. For electron Monte Carlo, to simulate the electron trigger, we require one B hadron in the event to have a $p_T > 14.0 GeV/c$ and $|\eta| < 1.0$. For the muon Monte Carlo, we demand one B hadron with $p_T > 14.0 GeV/c$ and $|\eta| < 0.6$. For both cases, we require a second B hadron with $p_T > 7.5 GeV/c$ and $|\eta| < 1.0$. The cuts placed on the generator-level Monte Carlo were determined by examining the p_T and η distributions for B hadrons from Monte Carlo events in which two BVTX tags were reconstructed. The p_T and η values were chosen by determining the cuts for which 90

In order to minimize the effect of statistical fluctuations in the tagging efficiency determined from Monte Carlo, we fit the tagging efficiency to an empirical function of the following form:

The relative efficiency curve resulting from this fit is shown in Figure XX. Since we are only interested in the effect of the efficiency on the shape of the $\Delta\phi$ distribution, and not on its absolute normalization, we have rescaled the curve in Figure XX so that the relative efficiency in the last $\Delta\phi$ bin is defined to be one. Thus this curve shows the effect of the BVTX tagging efficiency for a given bin relative to the last $\Delta\phi$ bin.

There are two main contributions to the systematic uncertainty associated with the relative tagging efficiency correction: First, the statistical errors on the fit value for the relative efficiency correction factor should be propagated into systematic uncertainties on the corrected $\Delta\phi$ distribution. There is an additional systematic uncertainty that comes from the model used to calculate the relative efficiency correction. The PYTHIA Monte Carlo sample, with PARP(67) = 4.0 and with the normalization of the different production mechanisms taken from the fit to the $\Delta\phi$ distribution in the data, is used as our baseline for the relative efficiency correction. However, other models, like the lower ISR PYTHIA sample or HERWIG also match the data to varying degrees and so could also have been used. To account for this ambiguity, we compare the relative efficiency corrections from other Monte Carlo models to our baseline model. In the worst case, the difference for the bin-by-bin relative efficiency correction factor is approximately equal in magnitude to the statistical error from the fit. Therefore, to account to modeling uncertainties in the relative efficiency correction, we increase the systematic error associated with the correction by a factor of $\sqrt{2}$.

H. Final Distribution and Comments

IV. J/ψ–LEPTON CORRELATION MEASUREMENT

A. Overview

This measurement is optimized to measure the region in phase space least understood in experimental measurements and theoretical predictions: small $\Delta\phi$ where both bottom quarks point in the same azimuthal direction. As stated previously, earlier bottom quark angular production measurements had little sensitivity to this region. A study of opposite side flavor tags using soft leptons for the CDF $\sin 2\beta$ measurement [28] showed an unexpected distribution between fully reconstructed bottom decays and the soft leptons. Figure 3 shows the sideband-subtracted $\Delta\phi$ distribution between $B^+ \to J/\psi K^+$ candidates and the soft leptons. $\sim 30\%$ of the soft leptons are in the same azimuthal hemisphere, a fraction much larger the expected from leading-log flavor creation Monte Carlo ($\approx 5\%$ for PYTHIA flavor creation).

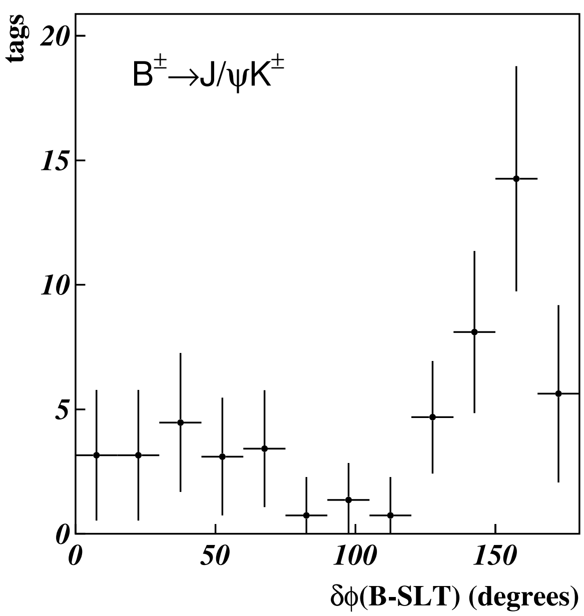

FIG. 3: Sideband-subtracted $\Delta\phi$ distribution between fully reconstructed $B^+ \to J/\psi K^+$ and soft leptons from ref. [28].

This analysis uses the bottom pair decay signature of $b \to J/\psi X, \bar{b} \to \ell^+ X$. The impact parameter of the additional lepton and the pseudo-$c\tau$ of the J/ψ are fit simultaneously in order to determine the $b\bar{b}$ fraction of the two $\Delta\phi$ regions. Angular requirements, that were necessary in previous di-lepton measurements due to double sequential semi-leptonic decay ($b \to c\ell X; c \to \ell X'$) are avoided by the chosen signal. B_c is the only particle that decays directly into J/ψ and an addition lepton. The only other source of candidates where the additional lepton and J/ψ candidates originate from the same displaced decay are hadrons that fake leptons or decay-in-flight of kaons and pions; the number of events from B_c or from 'fake' leptons can be estimated well by using techniques from ref. [29]. Thus, no angle requirement between the two candidate bottom decay products are necessary, yielding uniform efficiency over the entire $\Delta\phi^{b\bar{b}}$ range. Due to the limited size of the data sample, only f_{toward}, the fraction of $b\bar{b}$ pairs in the same azimuthal hemisphere, can be measured.

The selection criteria used in this analysis has similar bottom momenta and rapidity acceptances to CDF's Run II displaced track(SVT) [30] and J/ψ triggers, and the addition leptons have momenta very similar to the opposite side taggers planned for Run II (opposite kaon, opposite lepton and jet charge flavor taggers). Therefore, this measurement aids in the development and understanding of flavor taggers for such Run II measurements as the B_s mass difference.

B. Sample Selection

The signal searched for in this analysis is $b \to J/\psi X, \bar{b} \to \ell X'$ where ℓ can be an electron or muon. In this section, the Run 1B J/ψ data set is described. The off-line selection criteria for both the J/ψ and the additional lepton are also described.

1. $J/\psi \to \mu^+\mu^-$ Selection

This analysis uses the CDF Run 1b J/ψ data set obtained between January 1994 and July 1995. The CDF J/ψ triggers and off-line J/ψ selection criteria utilized are the same as the B_c discovery analysis at CDF [29]. In order to understand the trigger efficiencies, we confirm that the J/ψ candidate's muons are the two muon candidates which triggered the event.

After confirming the trigger, the position of the extrapolated track at the muon chamber is compared to the position of the muon stub using a χ^2 matching test, taking into account the effects of multiple scattering and energy loss in material. The positions are required to match within 3 standard deviations in the r–ϕ projection and within 3.5 standard deviations in the r–z projection.

Next, we require a high quality track for both muon candidates. The pseudo-lifetime ($c\tau$) of the J/ψ candidates is used in this analysis to determine the bottom purity. Therefore, SVX information is required in order to improve the precision of the $c\tau$ measurement.

In order to reject J/ψ candidates with muons originating from different primary interactions, the z position difference between the two tracks is required to be less than 5 cm at the beam-line. A vertex constrained fit of the two muon candidates is performed [31]. The χ^2 probability of the vertex fit is required to be better than

1%. The vertex constrained mass of the J/ψ candidate is required to be 2.9 GeV < $\mathrm{M_{J/\psi}}$ < 3.3 GeV.

A total of 177,650 events pass the above selection cuts. Figure 4 shows the J/ψ mass distribution for these events. In order to estimate the number of $J/\psi \rightarrow \mu^+\mu-$ candidates, the mass has been fit with two Gaussians (used to model the J/ψ signal) and a linear background term. A linear background has been assumed in many previous CDF J/ψ analyses [29, 32, 33]. The background under the mass peak is caused by: irreducible decay-in-flight and punch-though backgrounds, Drell-Yang muons and double sequential semi-leptonic decays where $b \rightarrow c\mu^- X, c \rightarrow s\mu^+ X'$. From the fit, 137780 ± 440 J/ψ candidates are in the sample. For this measurements, the J/ψ mass signal region is defined to be within ±50 MeV of the Particle Data Group's [34] world average value (3096.87 MeV). The sideband regions are chosen to be 2.900 GeV $\leq \mathrm{M_{J/\psi}} \leq$ 3.000 GeV and 3.200 GeV $\leq \mathrm{M_{J/\psi}} \leq$ 3.300 GeV. The sideband regions contain 20,180 events. The events in these regions are used later in the analysis to describe the $c\tau$ shape of fake J/ψ background in the mass signal region.

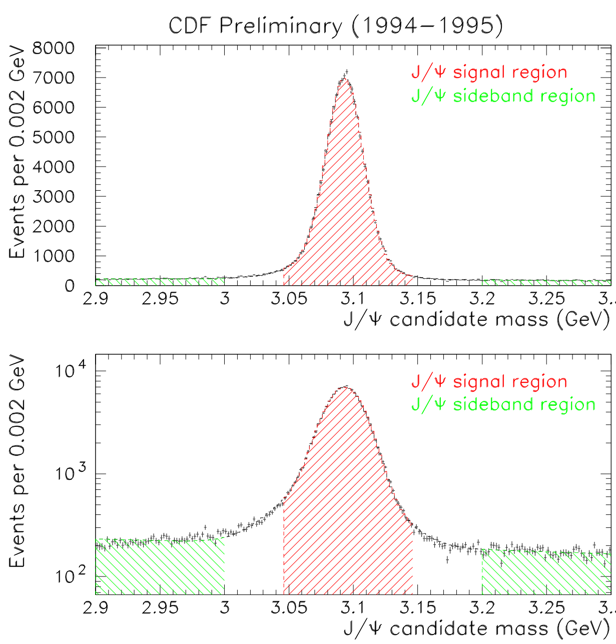

FIG. 4: Di-muon invariant mass distribution from events passing selection criteria. Top: Linear scale. Bottom: Logarithmic scale.

The ratio between the number of fake J/ψ events in the mass signal region to the mass sideband region (R_{side}) was determined to be $R_{side} = 0.501 \pm 0.000043$ by the mass fit. To estimate the systematic uncertainty of this ratio, a 2nd order polynomial is used to describe the background term. The resulting fit value is $R_{side} = 0.545 \pm 0.008$. The difference between the two fits is taken to be the systematic uncertainty yielding $R_{side} = 0.501 \pm 0.000043(\mathrm{stat}) \pm 0.044(\mathrm{syst})$.

2. *CMUP μ Selection Requirements*

The additional (non-J/ψ) muon is required to have muon stubs in both the CMU and CMP (a CMUP muon). Requiring both CMU and CMP muon stubs maximizes the amount of material traversed by the candidate, reducing the background due to hadronic punch-though of the calorimeter. The χ^2 matching requirements are the same as for the J/ψ muons. The muons candidates are required to have a $p_T > 3$ GeV; muons with lower p_T will typically range out prior to the CMP due to energy loss in the calorimeter and the CMP steel.

As the impact parameter is used to estimate the bottom purity of the muons, the same track quality is required as for the J/ψ muons. Additionally, the muon candidate's track projection is required to be in the fiducial volume of the CMU and CMP. The z positions of the J/ψ candidate and the CMUP muon are required to be within 5 cm of each other at the beam-line.

247 CMUP candidate muons are found in the J/ψ sample. 51(142) CMUP candidates are in events where the J/ψ candidate is in the mass sideband (signal) region.

Of the 142 CMUP candidates with J/ψ candidates in the J/ψ mass signal region, 64 events have the CMUP muon and the J/ψ candidate in the same hemisphere in the azimuthal angle (which will be known as toward); the other 78 events have the CMUP muon and J/ψ candidate in the opposite hemisphere in the azimuthal angle (which is denoted away).

3. *Electron Selection Criteria*

A method of the finding soft (relatively low momenta) electrons was developed for bottom flavoring tagging in CDF's B_d mixing and $sin(2\beta)$ measurements [27, 35]. These electrons have a relatively high purity, a transverse momenta greater than 2 GeV, and an understood efficiency. The rate of hadrons faking an electron was studied extensively in ref. [29], making it possible to estimate the background due to hadrons faking electrons. The selection criteria is identical to ref. [29] in order to use the same fake rate estimates.

The selection criteria requires a high quality track which is consistent with an electron in the various detector systems. Information on the energy (charge) deposited, the cluster location, and track matching χ^2 variables are all used in order to reduce the rate of a hadron in the detectors' fiducial volume faking an electron to $(6.4 \pm 0.6) \times 10^{-4}$.

One source of electron background is photon conversions, where a photon interacts with detector material and converts into a e^+e^- pair. In addition, 1.2% of all neutral pion decays into γe^+e^- directly (Dalitz decay).

To reduce this background, conversions are searched for and vetoed by looking for a conversion partner track.

The conversion requirements are the same as ref. [27]. Unfortunately, the conversion removal is not totally efficient. Therefore, some of the soft electron candidates are residual conversion electrons, where either the conversion pair track is not found due to tracking inefficiencies at low p_T or the conversion electron selection is not fully efficient. The rate of residual conversions is studied more in section IV C 4.

514 candidate electrons are found; 92 events have the J/ψ candidate in the mass sidebands and 312 events have the J/ψ candidate in mass signal region. 107(205) of the events with J/ψ in the mass signal region are in the toward(away) regions in $\Delta\phi$. In the J/ψ mass signal region, 6(9) events were vetoed as conversions in the toward(away) $\Delta\phi$ bin. In the J/ψ mass sideband region, 5(4) events were vetoed as conversions.

C. Signal and Background Description

The signal and backgrounds for both the $J/\psi + \mu$ and $J/\psi + e$ samples are very similar. The basic technique is to determine the amounts of the various signal and background components with a simultaneous fit of the pseudo-$c\tau$ (defined in section IV C 1) of the J/ψ and the signed impact parameter of the non-J/ψ lepton. The impact parameter is signed to distinguish between residual electron conversions and electrons from bottom decay, described more fully in section IV C 5. The impact parameter is signed positive if the primary vertex lies outside r–ϕ projection of the particle's helix fit.

As the J/ψ and additional lepton originate from separate bottom hadron decays, the impact parameter of the additional lepton and the $c\tau$ of the J/ψ are not strongly correlated for the signal. The backgrounds in this analysis have two categories: one in which the impact parameter and $c\tau$ are uncorrelated, and other where the impact parameter and $c\tau$ are strongly correlated. The impact parameter and the $c\tau$ become strongly correlated when both the J/ψ and the additional lepton candidate originate from the same displaced vertex.

In uncorrelated sources, the impact parameter and $c\tau$ shapes describing the background are determined independently. J/ψ candidates are assumed to originate from three sources: direct J/ψ production (including feed-down from χ_{c1}, χ_{c2}, and $\psi(2s)$) where the J/ψ decays at the primary vertex, J/ψ from bottom decay (including the feed-down from higher $c\bar{c}$ resonances), and the non-J/ψ background described by the events in the J/ψ mass sidebands. Leptons candidates are assumed to originate from the following sources: directly produced fake or real leptons from the primary vertex, leptons from bottom decay (including $b \to cX \to \ell X'$), lepton candidates with the fake J/ψ candidate, and residual conversion electrons.

In addition, two correlated sources of backgrounds exist. The first source is $B_c \to J/\psi \ell^+ X$, which is a small but irreducible background. The impact parameter of the additional lepton and the $c\tau$ of the J/ψ is described by Monte Carlos techniques and the overall size of the background is also estimated (see section IV C 7).

The other correlated source of background occurs when a bottom hadron decays into a J/ψ and a hadron which is mis-identified as a lepton. For electrons, this background is due to hadrons (mostly $\pi^{+/-}$ and $K^{+/-}$) showering early in the calorimeter and passing the electron identification selection. For muons, there are two sources of this background. The largest source of correlated background is due to decay-in-flight of charged pions and kaons, which result in a real muon. These real muons are denoted as 'fakes' in this analysis. The other, smaller correlated fake muon background is caused by hadrons punching-through the calorimeter and muon steel shielding. These background sources are more fully described in section IV C 8.

The following sections provide a description of the techniques used to determine the impact parameter and $c\tau$ shapes of the various sources and to estimate of the number of residual conversions, $B_c \to J/\psi \ell X$ events and $b \to J/\psi \ell_{\mathrm{fake}} X$ events in the sample.

1. J/ψ $c\tau$ Signal and Background Distributions

The direct J/ψ and bottom decay J/ψ $c\tau$ shapes are determined from a fit to the data, using a technique previously establish in ref. [32, 33]. The relatively long average lifetime of the bottom hadron ($(1.564 \pm 0.014) \times 10^{-12}$ s [34]) allows one to distinguish between these two sources. First, the signed transverse decay length L_{xy} is determined in the r–ϕ plane.

$$L_{xy} \equiv \frac{\left(\vec{X}_{SV} - \vec{X}_{PV}\right) \cdot \vec{p}_T^{\,J/\psi}}{p_T^{J/\psi}} \tag{2}$$

where $\vec{X}_{SV}$ and $\vec{X}_{PV}$ are the locations of the J/ψ and primary vertex in the transverse plane, and $\vec{p}_T^{\,J/\psi}$ is the vector transverse momentum of the J/ψ. Directly produced J/ψ have a symmetric distribution around zero and bottom J/ψ events will predominately have a positive sign. If the bottom decay was fully reconstructed, one could determine the proper decay length exactly ($c\tau_{proper}$) from the measured L_{xy} and p_T. Because the bottom hadron is not fully reconstructed, a 'pseudo-proper decay length' ($c\tau$) is constructed using the kinematics of the J/ψ only:

$$c\tau \equiv \frac{L_{xy} \cdot m_{J/\psi}}{p_T^{J/\psi} \cdot F_{corr}(p_T^{J/\psi})} \tag{3}$$

$F_{corr}(p_T^{J/\psi})$, determined in ref. [32], is the average correction factor for the partial reconstruction of the bottom hadron.

The events in the J/ψ mass sidebands are used in order to model the fake J/ψ background under the J/ψ mass signal peak. Two components are fit for using an unbinned log-likelihood technique: events from the primary vertex (direct) and events with lifetime from heavy flavor (predominantly from $b \to c\mu^- X \to \mu^+ X'$). The direct events are described by a symmetric resolution function chosen to be a Gaussian plus 2 symmetric exponentials. The events with lifetime are fit with a positive only exponential.

Once the $c\tau$ shape of the mass sideband event is found, the $c\tau$ shapes of directly produced and bottom decay J/ψ can be determined. The shape of the directly produced J/ψ ($F^{c\tau}_{direct}(x)$) is parameterized by a Gaussian with two symmetric exponential tails; this shape is the assumed resolution function of the $c\tau$ measurement. The shape of J/ψ events from bottom decay ($F^{c\tau}_{b}(x)$) is therefore described as a positive exponential convoluted with the $c\tau$ resolution function. The background shape (g_{back}) is fixed to the value obtained in the fit of the sideband region and the background fraction (f_{back}) is fixed to the value predicted by the J/ψ candidate mass fit. Figure 5 shows the fit result of the signal region. The fit average bottom proper decay length of 442 ± 5 μm is consistent with previous measurements at the Tevatron [32, 33]. The fit yields a bottom fraction of $16.6\% \pm 0.2\%$ or equivalently 22150 ± 270 J/ψ from bottom decay.

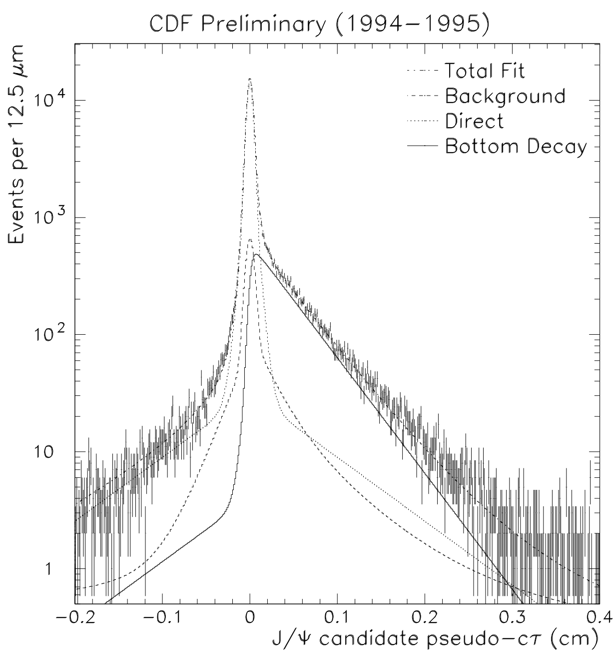

FIG. 5: Fit of J/ψ signal region.

2. Lepton Impact Parameter Signal Distributions

The impact parameter shape of bottom decay leptons is determined by Monte Carlos simulation, using the prescription from ref. [19] for leading-log order showering Monte Carlos. In this prescription, separate samples of flavor creation, flavor excitation, and gluon splitting Monte Carlos are generated and then combined with the relative rates predicted by the Monte Carlos. In appendix A, the generation of the simulated events is described.

Figure 6 shows the unsigned impact parameter for direct bottom electrons ($b \to ce^-$) and sequential charm electrons ($b \to c \to se$) in the flavor creation Monte Carlos. The impact parameter distributions are very similar and cannot be fit for separately. The sequential fraction given by the Monte Carlos is used in the analysis, and the uncertainty on the sequential fraction is one of the systematic uncertainties treated in section IV D 1. The bottom decay impact parameter shape is fit with two symmetric exponentials and a Gaussian. The fit to the simulated bottom impact parameter distribution for electrons is shown in fig. 7.

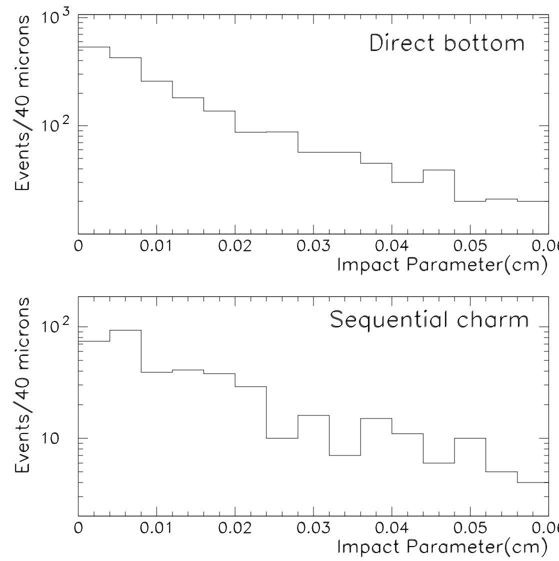

FIG. 6: The impact parameter of events with electrons passing requirement in the flavor creation Monte Carlo sample. Top: Direct bottom. Bottom: Sequential charm.

3. Lepton Impact Parameter Background Distributions

In previous analyses [11, 12], the impact parameter distributions for particles originating at the primary vertex was determined using jet data. Unfortunately, any data sample will have low level contamination of heavy

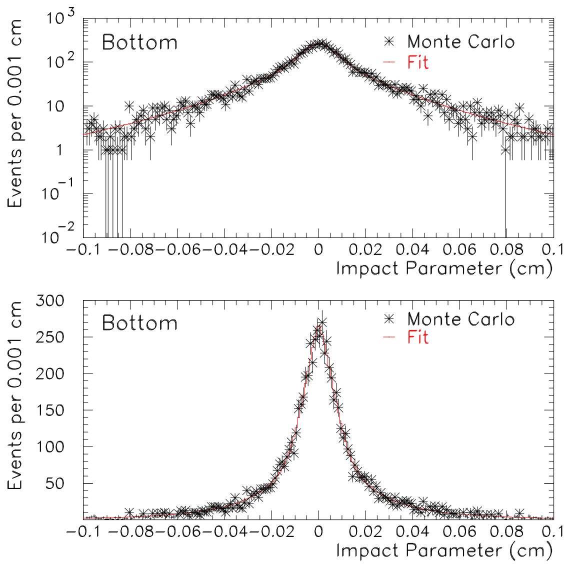

FIG. 7: The signed impact parameter distribution for the combined electron bottom Monte Carlos. Top: Logarithmic scale. Bottom: Linear scale.

flavor (charm or bottom) at the $\approx 0.1 - 1\%$ level, which is larger than the non-Gaussian effects in the impact parameter resolution. In this analysis, the impact parameter shapes of directly produced particles are determined with a Monte Carlos technique.

PYTHIA is used to generate the light quark and gluon subprocesses, which is then passed through a detector simulation. To be included in the electron direct shape, the candidates must be a quality track with a $p_T > 2$ GeV and extrapolate into the electron fiducial region. For the muon direct shape, the candidates must be a quality track with a $p_T > 3$ GeV and extrapolate into the CMUP muon fiducial region. The Monte Carlos events which pass the selection criteria are fit with two symmetric exponentials and a Gaussian. The fit shapes are then used as input to the likelihood fit for particles originating from the primary vertex (direct tracks).

4. Size of Residual Conversion Background

One obvious source of electron background is residual conversions left in the sample, due to the inefficiency of finding the conversion pair. In order to estimate the number of residual conversions, a technique similar to ref. [36] is used. In the technique, one assumes that there are two independent causes for the lack of removal of a conversion electron: the track pair is lost due to tracking inefficiencies at low momenta or the selection requirements are not fully efficient. By measuring these two efficiencies and the rate of conversion removal with the chosen conversion selection requirements, one determines the residual electrons (N_{resid}). The conversion electron that passes the electron identification criteria is denoted as the SLT conversion candidate, and other electron that did not pass the electron identification criteria is denoted as the pair candidate.

The number of residual electrons is equal to:

$$N_{resid} = N_{tag} \cdot \left(\frac{1}{\epsilon_{cnv}(cut)} \cdot \frac{1}{\epsilon_{cnv}(p_T)} - 1 \right) \qquad (4)$$

where:
N_{tag} is the number of the conversions removed, $\epsilon_{cnv}(cut)$ is the conversion finding efficiency, and $\epsilon_{cnv}(p_T)$ is the tracking efficiency of the conversion pair.

$\epsilon_{cnv}(cut)$ is measured using different sets of conversion requirements, the standard (tight) and a loose set cuts. Assuming that the loose cuts are fully efficient, the number of conversion pairs fit with tight and loose cuts yields $\epsilon_{cnv}(cut) = 72.3 \pm 6.5\%$. In order to test this assumption, 2 additional wider sets of cuts are used which yield no extra conversion candidates.

The tracking efficiency of the pair candidates ($\epsilon_{cnv}(p_T)$) is estimated with a Monte Carlos technique similar to ref. [29]. The generation of the simulated conversions is detailed in section A. $\epsilon_{cnv}(p_T)$ is estimated by comparing the Monte Carlos truth information of the conversion partner to the p_T of the conversion partners found in data. The simulation is normalized to the data in the p_T range where the tracking is fully efficient ($p_T > 0.5$ GeV). The ratio of the number of events seen in data versus the number of normalized conversion candidates in Monte Carlo is the estimate of $\epsilon_{cnv}(p_T) = 69 \pm 5(\text{stat}) \pm 9(\text{syst})\%$. The systematic error includes the uncertainty in the p_T spectra of the primary pions.

The ratio of the number of residual to found conversions was found to be $R_{conv} = 1.00 \pm 0.38$. The conversion veto removes 6(9) SLT electron candidates in the toward(away) $\Delta\phi$ region. Thus, approximately 6.0(9.0) residual conversion are in toward(away) $\Delta\phi$ region . About 5% of the SLT electron candidates are residual conversions and have to be included in the $c\tau$–impact parameter fit. A total of 9 conversions (4 toward, 5 away) are found in events with the J/ψ candidate in the mass sideband region.

5. Impact Parameter Shape of Residual Conversion Background

For conversion electrons from a primary photon, the primary vertex alway lies outside of the helix projection with perfect tracking. To distinguish between conversions and bottom decay electrons, the impact parameter is signed such that the impact parameter as positive if the primary vertex is outside the r-ϕ projection of the track's helix, and the sign of the impact parameter is negative otherwise. Conversion electrons are positively signed, and Dalitz decay electrons and bottom decay electrons are equally negatively and positively signed.

The vast majority of the conversion candidates are signed positive as predicted (shown in fig. 8). Unfortunately, there is a large positive tail which is not consistent with the number of SVX hits assigned to the track. Since at least 3 SVX hits are required, one would expect the conversion candidates are either originate from the first two SVX layers or the beam pipe, or be a π^0 Dalitz decays from the primary vertex. These sources would produce conversions with a impact parameter less than 0.04 cm. Therefore, a fraction of the conversion candidates must have mis-assigned SVX hits and originate outside of the SVX. The measured conversion radius for 25 of the 62 conversion candidates have a radius greater than 6 cm, which is outside of the second SVX' layer.

To construct an impact parameter shape for residual conversions, two Monte Carlos samples are generated: a sample in which the SVX hit are correctly assigned (low conversion radius, $R_{conv} < 6$ cm), and a component which which SVX hits are falsely added (mostly at high conversion radius, $R_{conv} > 6$ cm)). The relative fractions of the two components are determined by data. The fraction of conversions with $R_{conv} < 6$ cm ($f^{GoodSVX}_{conv}$) in data and Monte Carlos are matched, with the uncertainty in the fraction in data included as a systematic uncertainty in the shape.

Figure 8 shows the impact parameter of the candidates found in data and the combined conversion impact parameter shape normalized to data. The combined impact parameter shape describes the data well, including both the negative tail and large positive tail.

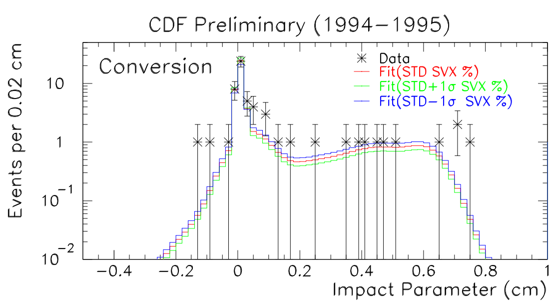

FIG. 8: The signed impact parameter distribution for conversions found in data. Red: Monte Carlos fit using the central value of $f^{GoodSVX}_{conv}$. Green: Monte Carlos fit increasing $f^{GoodSVX}_{conv}$ by one sigma. Blue: Monte Carlos fit decreasing $f^{GoodSVX}_{conv}$ by one sigma.

6. *Additional Lepton Impact Parameter Distributions in Events with Fake J/ψ*

Events in which the J/ψ candidate is in the mass sideband regions are used to describe the impact parameter shape of leptons in events with a fake J/ψ. The composition of events in the J/ψ mass sidebands are unknown; therefore, the shapes have to be fit in a similar manner as section IV C 1.

For the muon sample, there is no knowledge of the contributions to the addition muon's impact parameter distribution. Therefore, the shape has to be parameterized with a Gaussian and and symmetric exponential.

The sideband impact parameter shape in the electron sample has an additional complication; the electron sample's sideband contains residual conversions. The number of found conversions in the signal region is used as a constraint on the number of residual conversion events in the signal region. Thus, the number of residual conversion events fit in the sideband region has to be known. In the sidebands, the residual conversion fraction is fit for $f_{conv} = \frac{r_{conv} \cdot n_{convside}}{N_{sideband}}$, where r_{conv} and $n_{convside}$ are the fit ratio of residual to found conversions and fit number of "found" conversions, respectively. These quantities are constrained by the estimate of R_{conv} and the number of found conversions in the sidebands, $N_{convside}$. Since r_{conv} is a component of the signal region fit, the signal and sideband regions have to be fit simultaneously.

7. *$B_c \to J/\psi\ell^+X$ Background*

B_c decay is the only known process that yields a lepton and a J/ψ from the same displaced vertex. CDF's measurement [29] of the $\frac{\sigma(B_c)\cdot BR(B_c \to J/\psi\ell\nu)}{\sigma(B^+)\cdot BR(B^+ \to J/\psi K)}$ and the B_c lifetime allow one to estimate both the number and impact parameter–$c\tau$ shape of this background. The estimated number of $B_c \to J/\psi\ell X$ events in the samples is used as a constraint in the fit.

Taking into account correlated uncertainties, the number of $B_c \to J/\psi\ell X$ events estimated in the sample are $N^e_{B_c} = 10.0^{+3.5}_{-3.3}$ and $N^\mu_{B_c} = 7.2^{+2.6}_{-2.4}$. According to Monte Carlo, over 99% of the B_c passing the selection requirements have $\Delta\phi < \frac{\pi}{2}$ between the lepton and the J/ψ. Thus, this background is only fit for in toward $\Delta\phi$ region in the measurement.

Using a $B_c \to J/\psi\ell\nu$ Monte Carlo sample described in section A, the impact parameter–$c\tau$ shape is determined. The shape takes into account the correlation in the impact parameter of the addition lepton and the $c\tau$ of the J/ψ. As the $c\tau$ of the J/ψ increases, the impact parameter of the additional lepton can be larger.

8. *$b \to J/\psi\ell_{fake}$ Background*

The other source of background where the impact parameter and $c\tau$ are correlated is bottom hadrons decaying to a real J/ψ with a hadron from the same decay faking an lepton. The sources and rates for faking leptons were studied extensively in ref. [29] and are used in this analysis. In Monte Carlos, more than 99% of the events have the J/ψ and the fake lepton candidate in the same azimuthal hemisphere, and therefore this background is only fit for in the toward $\Delta\phi$ region.

The estimates of the amount and shapes of these backgrounds are made using a Monte Carlos sample of $b \to J/\psi X$ events, described in section A. Hadrons can "fake" an electron by showering early in the calorimeter. "Fake muons" can be caused by decay-in-flight of charged pions and kaons, and by hadrons not being completely absorbed in the calorimeter and leaving hits in the muon chamber.

The rate that a hadron will fake an electron was studied in ref. [29]. The number of $b \to J/\psi e_{\rm fake} X$ events is determined by using these fake rates and the Monte Carlos sample. To be included in the fake rate calculation, an event must pass the J/ψ selection and have an charged hadron in the electron identification fiducial with a track with SVX hits and a $p_T > 2$ GeV. Ideally, one then would apply the appropriate fake rate for the particle's p_T and isolation for each track passing the selection, yielding the total fake rate. Unfortunately, the Monte Carlos used does not include particles from the underlying event, fragmentation, gluon radiation or the other bottom hadron in the event. Thus, the isolation in the simulation does not represent the data. A large fraction ($\sim 70\%$) of the events have a small isolation ($I < 0.2$); this value of the isolation value is used as a central value of the estimate. The other fake rates are used to quantify the systematic uncertainty of the background estimate.

Normalizing the Monte Carlo to the estimated number of $b \to J/\psi X$ events in data yields a estimate of $2.85 \pm 0.03(\text{stat.}) \pm 0.75(\text{isolation})$ events, where the second error is the systematic uncertainty due to modeling (or lack of) of the track isolation.

The impact parameter-$c\tau$ shape of this background is determined by a fit to the Monte Carlos. The Monte Carlos sample used in the fit are events which can included in the electron fake rate calculation.

Decay-in-flight(DIF) of charged pions and kaons to muons is also a source of correlated background, as long as the track is reconstructible. The probability of a decay-in-flight to have a reconstructible track is greatly reduced by the SVX requirements, as shown in ref. [29].

The number of correlated background events from decay-in-flight is determined in a manner similar to the fake electron estimate. The Monte Carlos is normalized in the same manner as the fake electron calculation. The J/ψ candidate is required to pass the selection criteria in section IV B 1, and the decay-in-flight candidates are required to have a SVX track with $p_T > 3$ GeV and project into the CMU and CMP fiducial volumes. The probability of decaying-in-flight is determined for the given p_T and particle species. $64.2 \pm 0.3\%$ of the particles passing the requirements are kaons. The decay-in-flight background is estimated to average 9.9 ± 2.1 events. The error includes the 12% Monte Carlos calculation systematic uncertainty and a 17% reconstruction efficiency systematic uncertainty quoted in ref. [29].

In ref. [29], the decay-in-flight estimate was done using data. In that analysis, the kaon fraction was measured to be $(44 \pm 4.4)\%$. The difference between the kaon fraction in ref. [29] and the simulation could lead to a large systematic difference, because of the difference in the kaon and pion decay-in-flight probabilities. To estimate this uncertainty, the Monte Carlos events are reweighted in order to match the kaon fraction measured by [29]. With the re-weighting, the estimated number of correlated decay-in-flight background is estimated to be 8.7 ± 2.0. The difference between the two estimates is conservatively used as the systematic error, yielding a final decay-in-flight estimate of $N^{\mu,DIF}_{B_{fake}} = 9.9 \pm 2.4$.

The impact parameter–$c\tau$ shape of the decay-in-flight background is determined by the same Monte Carlos sample. In ref. [12, 29], it is shown that the impact parameter distribution of reconstructible decay-in-flight particles with SVX information have the same impact parameter distribution of the parent particle. Similar to the fake electron shape, the Monte Carlos events which could be used in the DIF rate calculation are fit in order to determine the DIF impact parameter–$c\tau$ shape.

Hadrons can also mimic muons by not being completely absorbed by the calorimeter and leaving hits the muon chambers. The probability of a track punching-through the calorimeter was determined in ref. [29]. The selection criteria of the punch-through estimate is the same as the the decay-in-flight estimate. The punch-though probability of the tracks passing the requirements is calculated from its particle type and momentum, yielding the final estimate. An average 1.76 ± 0.70 punch though events are expected in the data, including a 40% systematic error used in [29].

As the punch-though rate is much larger for K^+ than K^- or $\pi^{+/-}$, the large difference in kaon fraction between [29] and Monte Carlos (shown in the decay-in-flight estimate) is a significant systematic shift in the punch-through estimate. To be conservative, we reweight the data with the kaon fraction measured in ref. [29]; 1.23 ± 0.46 events are expected. The difference between the two predictions is used as the estimate of the systematic uncertainty in the prediction, yielding a final estimate of the average number of correlated backgrounds from punch-through of $N^{\mu,PT}_{B_{fake}} = 1.76 \pm 0.88$ events. In ref. [37], the decay-in-flight and punch-through backgrounds are shown to have the same lifetime shape in the B_c lifetime fit. The decay-in-flight and punch-through backgrounds are assumed to have the same impact parameter–$c\tau$ shape.

D. Unbinned Likelihood Fit Results

An unbinned log-likelihood fit is used to determine the estimate number of $b\bar{b}$ pairs and backgrounds in the two $\Delta\phi$ regions. The fit uses as inputs the J/ψ's $c\tau$, the additional lepton's impact parameter, and shapes and background estimates described in the previous sections. The shapes are used to determine the sample compositions, with the background estimates used as constants. In appendix B, the complete details of the log-likelihood function is given.

The log-likelihood ($-2\ln\mathcal{L}$) is minimized for both data sets using MINUIT [38]. The fit parameter errors are defined by $\pm1\sigma$ ($\Delta\mathcal{L} = 1$) contours of the likelihood function using the MINOS option. The results of the fit are shown in table I. In order to display the fit result, the log-likelihood function has been integrated in regions of impact parameter–$c\tau$ space. As examples of the fit quality, figures 9 and 10 show the fit results projected onto the impact parameter and $c\tau$ axis for the electron sample in the away $\Delta\phi$ region and muon sample in the toward $\Delta\phi$ regions, respectively.

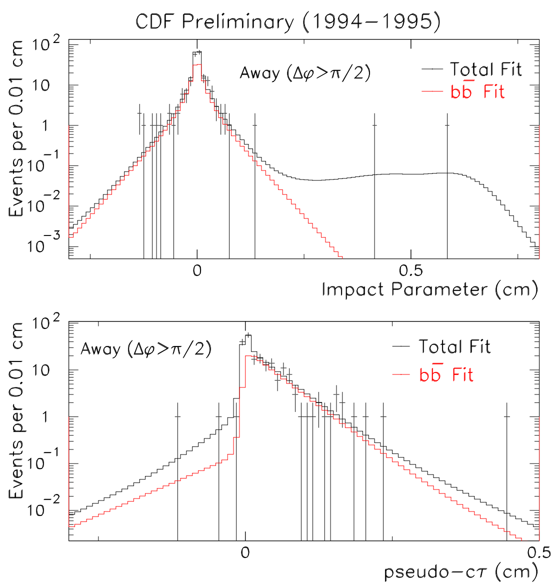

FIG. 9: Result of the $c\tau$–impact parameter fit for the electron sample in the away bin. Top: Projection onto impact parameter axis. Bottom: Projection onto $c\tau$ axis.

The toward fraction measured in the two samples are:

$$f^{\mu}_{toward} = 34.5^{+9.2}_{-8.2}\% \quad (5)$$
$$f^{e}_{toward} = 19.2^{+6.5}_{-5.9}\% \quad (6)$$

The measurement error includes both the statistical error as well as systematic uncertainties due to the constraints.

As a test of the fitting technique, a set of 1000 toy Monte Carlos 'experiments' have been generated. The results of the study, given in appendix C, show that the fit results are unbiased and have proper errors.

1. *Fit Systematics*

By measuring the fraction of bottom quark pairs produced in the same hemisphere f_{toward}, the systematic

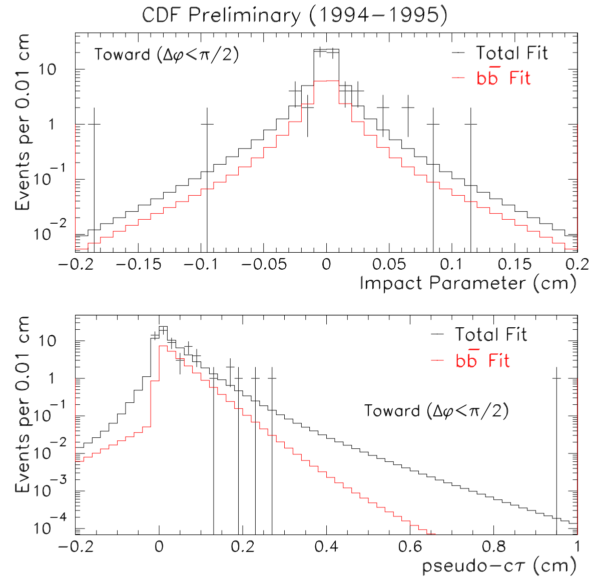

FIG. 10: Result of the $c\tau$–impact parameter fit for the muon sample in the away bin. Top: Projection onto impact parameter axis. Bottom: Projection onto $c\tau$ axis.

uncertainties are minimized. The selection in both the $\Delta\phi < \pi/2$ and $\Delta\phi > \pi/2$ regions are the same; therefore, the uncertainties in the lepton selection efficiency, tracking efficiency, luminosity, etc. mostly cancel in the fraction measurement. In this section, the systematic uncertainty in the log-likelihood not already included in the fit is estimated. The estimated size of these systematic uncertainties are collected in table II.

The sequential charm fraction (f_{seq}) that is used in the bottom impact parameter shape ($F^{d_0}_b$) is derived by the simulation. The uncertainty in the sequential charm fraction leads to a systematic uncertainty in the determination of $F^{d_0}_b$, as sequential charm leptons have a larger impact parameter than direct bottom leptons. In ref. [12], the relative systematic uncertainty in f_{seq} was studied. The relative uncertainty is f_{seq} was $\pm19\%$, which is used in this analysis. f_{seq} is varied by $\pm1\sigma$, $F^{d_0}_b$ is re-fit, and then the new $F^{d_0}_b$ shapes are then used to re-fit f_{toward}. The maximum differences of $\pm0.1\%$ and $\pm0.3\%$ are assigned as the systematic uncertainty for the electron and muon samples,respectively.

The bottom hadrons' lifetimes (B^+, B^0, B_s, and Λ_b) and their decay products' impact parameters are strongly correlated. In order to estimate the uncertainty caused by bottom lifetime uncertainty, two additional Monte Carlos samples were generated using BGENERATOR [39], a fast $b\bar{b}$ Monte Carlos that approximates the NLO prediction by ref. [1]. All the bottom hadrons lifetimes are shifted by $\pm1\sigma$ from their PDG values [34]. The $F^{c\tau}_b$ shapes determined by these samples are then used in a re-fit of f_{toward}. The estimate of the system-

Fit parameter	Electron	Electron Constraint	Muon	Muon Constraint
$n^t_{b\bar{b}}$	$29.6^{+11.7}_{-10.4}$		$23.0^{+7.6}_{-6.9}$	
n^t_{bd}	$1.5^{+8.5}_{-8.1}$		$1.6^{+4.6}_{-2.9}$	
n^t_{bconv}	0.6(fixed)		N/A	
n^t_{db}	0 (fixed)		0 (fixed)	
n^t_{dd}	$37.0^{+8.0}_{-7.3}$		$11.3^{+5.1}_{-4.5}$	
n^t_{dconv}	$2.8^{+2.1}_{-1.7}$		N/A	
n^t_{side}	$45.4^{+6.9}_{-6.2}$	45	$32.9^{+5.7}_{-5.1}$	34
$n^t_{B_{fake}}$	$2.8^{+0.7}_{-0.7}$	2.85 ± 0.75	$10.7^{+2.5}_{-2.5}$	11.7 ± 2.6
$n^t_{B_c}$	$10.0^{+3.2}_{-3.3}$	$10.0^{+3.5}_{-3.3}$	$5.1^{+2.5}_{-2.5}$	$7.2^{+2.6}_{-2.4}$
n^t_{signal}	107.1	107	68.2	64
n^t_{conv}	5.6	6	N/A	
$n^a_{b\bar{b}}$	$124.7^{+17.9}_{-16.7}$		$43.6^{+10.2}_{-9.0}$	
n^a_{bd}	$-1.4^{+12.5}_{-12.2}$		$8.1^{+8.0}_{-7.5}$	
n^a_{bconv}	1.2(fixed)		N/A	
n^a_{db}	0 (fixed)		0 (fixed)	
n^a_{dd}	$49.5^{+9.2}_{-8.5}$		$16.0^{+5.5}_{-5.2}$	
n^a_{dconv}	$6.0^{+2.6}_{-2.2}$		N/A	
n^a_{side}	$47.6^{+7.1}_{-6.5}$	47	$18.2^{+4.5}_{-3.9}$	17
n^a_{signal}	204.9	205	76.8	78
n^a_{conv}	9.5	9	N/A	
r_{side}	$0.505^{+0.043}_{-0.0043}$	0.501 ± 0.44	$0.501^{+0.043}_{-0.043}$	0.501 ± 0.044
r_{conv}	$0.99^{+0.31}_{-0.28}$	1.00 ± 0.37	N/A	

TABLE I: Fit results and constraints for the electron and muon samples. n_{signal} and n_{conv} are not fit parameters but are functions of fit parameters.

atic uncertainty due to the bottom lifetime is chosen to be the greatest differences from the standard fit. ±0.3% and ±2.2% are the uncertainties estimated in the electron and muon samples.

B_s, B^+, and B^- have proper decay lengths of $\sim$ 470 μm, whereas Λ_B has a proper decay length of 387 μm. Thus, the uncertainty in the fraction of bottom quarks fragmenting to Λ_b leads to the largest uncertainty of the $F^{c\tau}_b$ shape. Using BGENERATOR, samples are generated with the Λ_b fragmentation fraction varied by $\pm 1\sigma$ from the PDG values [40] . The new $F^{c\tau}_b$ shapes are used to re-fit f_{toward}, with the maximum difference from the standard fit used as the estimate of the systematic uncertainty, yielding a systematic uncertainty of ±0.1% and ±0.2% for the electron and muon samples.

Due to the limited number of residual conversions in the sample, the number of conversions pairing with J/ψ for bottom decay (n_{bconv}) and with direct J/ψ (n_{dconv}) cannot be fit independently. Thus, the ratio between n_{bconv} and n_{dconv} is fixed to the fit ratio between J/ψ from bottom decay and directly produced J/ψ. In order to estimate the systematic uncertainty due to this assumption, the fit of the data is re-done with either n_{bconv} or n_{dconv} fixed to zero; the difference between fits are used as an estimate of the systematic uncertainty, yielding a systematic uncertainty of ±0.1% for the electron sample.

The residual conversion shape (F_{conv}) is determined using data and simulation. In data, the conversion radii of the found conversions indicate that a large fraction of the conversion candidates have at least 1 SVX hit misassigned to the track. F_{conv} is the sum of two shapes: $F^{GoodSVX}_{conv}$, which describes the shape of residual conversion where SVX hits are assumed to be correctly assigned, and F^{BadSVX}_{conv}, which describes the shape of residual conversion where at least 1 SVX hit is assumed to be incorrectly assigned. $F^{GoodSVX}_{conv}$ and F^{BadSVX}_{conv} are determined using Monte Carlos in section IV C 5. The value of $f^{GoodSVX}_{conv}$ is changed by $\pm 1\sigma$ in F_{conv} in order to estimate the systematic uncertainty due to the F_{conv} shape used. The maximum difference of ±0.2% is assigned as a conservative estimate of the systematic uncertainty due to the residual conversion impact parameter shape used.

The direct impact parameter shapes ($F^{d_0}_{direct}$) are determined by a fit to Monte Carlos samples in section IV C 3. The finite size of the Monte Carlos samples lead to an uncertainty in the fit parameters of the shapes. In order to estimate the uncertainty in f_{toward} due the $F^{d_0}_{direct}$

Source	Electron	Muon
Sequential Rate	$\pm 0.1\%$	$\pm 0.3\%$
B Lifetime	$\pm 0.3\%$	$\pm 2.2\%$
Fragmentation Fractions	$\pm 0.1\%$	$\pm 0.2\%$
n_{bconv}/n_{dconv} ratio	$\pm 0.1\%$	
Residual Conversion Shape	$\pm 0.2\%$	
Direct Impact Parameter Shape	$^{+0.3}_{-0.4}\%$	$^{+7.4}_{-1.0}\%$
f_{back} (for $F^{c\tau}_{Direct}$ and $F^{c\tau}_{b}$)	$\pm 0.02\%$	$\pm 0.01\%$
N_{db}	$\pm 0.1\%$	$\pm 1.9\%$
Total	$^{+0.5}_{-0.6}\%$	$^{+8.0}_{-3.1}\%$

TABLE II: Summary of the estimated values of the systematic uncertainty for f_{toward}.

shape uncertainty, each parameter is fixed to a value $\pm 1\sigma$ from the best fit value and the $F^{d_0}_{direct}$ shape is re-fit. The new shape is then used in the impact parameter–$c\tau$ fit. The largest negative and positive differences from the standard fit is conservatively assigned as the systematic error, $^{+0.3}_{-0.4}\%$ for the electron sample and $^{+7.4}_{-1.0}\%$ for the muon sample.

The direct and bottom $c\tau$ shapes are determined by a fit to the data. In the fit, the fraction of fake J/ψ events (f^{back}) is fixed at the predicted fraction. In order to estimate the effect on f_{toward}, the value of f^{back} is change by $\pm 1\sigma$ and the J/ψ mass signal region $c\tau$ fit is re-done. The resulting $F^{c\tau}_{direct}$ and $F^{c\tau}_{b}$ shapes are used in a re-fit of f_{toward}. The greatest difference from the standard fit is chosen to be a conservative estimate of systematic uncertainty, yielding uncertainty estimates of $\pm 0.015\%$ and $\pm 0.01\%$ for the electron and muon channels.

In this analysis, the number of events with a directly produced J/ψ with a lepton from bottom decay (n_{db}) is assumed to be zero. In order to measure the effects of this assumption, a fit of f_{toward} is performed where n_{db} is a free parameter. The difference in this fit from the standard fit is assigned as the systematic uncertainty due to n_{db}. We assign a $\pm 1.9\%$ uncertainty to f^{μ}_{toward} and $\pm 0.1\%$ to f^{e}_{toward}.

The individual systematic uncertainties are added in quadrature in order to determine the combined systematic uncertainty. The systematic uncertainties for the electron and muon samples are $^{+0.5}_{-0.6}\%$ and $^{+8.0}_{-3.1}\%$, respectively.

2. *Correction to b quark level*

At this time, no fragmenting, NLO QCD calculation of bottom production at the Tevatron exists . In order to compare to next-to-leading order calculations, one must 'correct' the experimental measurement to the bottom quark level (f^{corr}_{toward}), using similar technique as in Ref. [11, 12, 41].

Sample	$p_T^{J/\psi}$	$y^{J/\psi}$	p_T^{e}	y^{e}
FC	6.8 GeV	0.66	5.3 GeV	0.98
FE	7.1 GeV	0.66	3.8 GeV	1.06
GS	6.4 GeV	0.70	3.8 GeV	0.92
Ave	6.8 GeV	0.67	4.3 GeV	0.99

Sample	$p_T^{J/\psi}$	$y^{J/\psi}$	p_T^{μ}	y^{μ}
FC	7.3 GeV	0.66	6.6 GeV	0.60
FE	7.0 GeV	0.66	5.8 GeV	0.66
GS	6.6 GeV	0.68	5.7 GeV	0.58
Ave	7.0 GeV	0.67	6.0 GeV	0.61

TABLE III: 90% acceptance requirements on the bottom quarks decaying to a J/ψ or a lepton predicting by PYTHIA Monte Carlos and a detector simulation. Top: Electron. Bottom: Muon.

The correction is:

$$C_{B\rightarrow b} = \frac{f^{b\bar{b}\ \ 90\%}_{toward,mc}}{f^{b\rightarrow J/\psi X;\bar{b}\rightarrow \ell Y}_{toward,mc}} \tag{7}$$

$f^{b\rightarrow J/\psi X;\bar{b}\rightarrow \ell Y}_{toward,mc}$ is the f_{toward} prediction by PYTHIA, where the $\Delta\phi$ is calculated between the J/ψ and the additional lepton, which both meet the selection criteria. The distributions of the p_T and rapidity (y) of bottom quarks in Monte Carlos events that pass J/ψ and lepton selection (shown in figure 11–12) are used to determine the p_T and rapidity regions for the calculation of the correction factor. $p_T^{J/\psi}$ is defined to be the value of the bottom quark transverse momentum in which 90% of the b quarks which decay to a J/ψ have a higher momenta. $y^{J/\psi}$ is defined to be the value of bottom quark's $|y|$ in which 90% of the b quarks which decay to a J/ψ have a lower $|y|$. p_T^{ℓ} and y^{ℓ} are defined in a similar manner for the bottom quark that decayed into the additional lepton. Table III shows the value determined in both the electron and muon samples for three different production mechanisms. The rapidities of all three mechanisms are very similar and are determined by the detector geometry. The p_T values are different in the three mechanisms. Flavor creation produces two bottom quarks with similar momenta, while gluon splitting and flavor excitation produce quarks with dissimilar p_T. The values of $y^{J/\psi}$, y^{ℓ}, $p_T^{J/\psi}$, and p_T^{ℓ} used in the correction factor calculation is the average of the three production mechanisms. To estimate the size of the systematic uncertainty, $C_{B\rightarrow b}$ is calculated for each production mechanism separately. The systematic uncertainty is estimated as the largest difference between the individual and combined production mechanisms.

$f^{b\bar{b}\ \ 90\%}_{toward,mc}$ is the fraction of bottom quarks produced by PYTHIA in the same hemisphere which pass the following criteria:

- $p_T^{b_1} > p_T^{J/\psi}$ and $|y^{b_1}| < y^{J/\psi}$

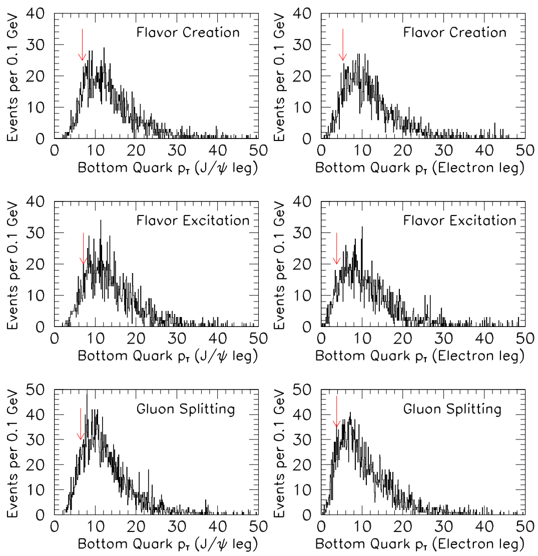

FIG. 11: p_T of the bottom quarks in events that pass selection in the electron PYTHIA samples. The arrows indicate the 90% acceptance value.

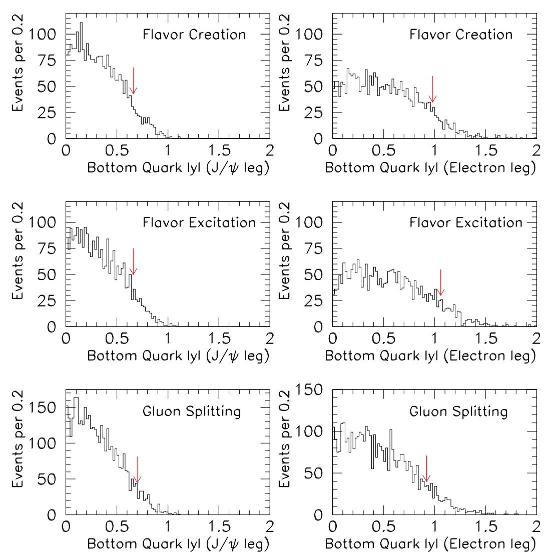

FIG. 12: $|y|$ of the bottom quarks in events that pass selection in the electron PYTHIA samples. The arrows indicate the 90% acceptance value.

- $p_T^{b_2} > p_T^{\ell}$ and $|y^{b_2}| < y^{\ell}$

$b_{1,2}$ can be either the bottom quark or antiquark. No requirements are made on the decay products of the bottom quarks. Table IV shows the $f_{toward,mc}^{b\bar{b}\ 90\%}$, $f_{toward,mc}^{b\to J/\psi X;\bar{b}\to \ell Y}$, and $C_{B\to b}$ for the complete sample and the three separate production mechanisms. The values estimated are:

$$C^{e}_{B\to b} = 0.967 \pm 0.019(\text{stat.}) \pm 0.088(\text{syst.}) \quad (8)$$
$$C^{\mu}_{B\to b} = 0.968 \pm 0.026(\text{stat.}) \pm 0.061(\text{syst.}) \quad (9)$$

The measured toward fraction for the bottom quarks (f_{toward}^{corr}) extracted using the correction factor ($C_{B\to b}$) is:

$$f_{toward}^{corr,e} = 18.6^{+6.3}_{-5.7}\,{}^{+0.5}_{-0.6} \pm 1.7\% \quad (10)$$
$$f_{toward}^{corr,\mu} = 33.4^{+8.9}_{-7.9}\,{}^{+7.7}_{-3.0} \pm 2.3\% \quad (11)$$

where the first error is the fit error, the second error is the additional shape systematic uncertainties on f_{toward}, and the third error is the uncertainty due to the correction to the bottom quark kinematics.

E. Data–Theory Comparisons

The measured toward fraction corrected to the quark level is compared to the NLO QCD predictions [1], using the same requirements as for the correction of the experimental measurements. The NLO prediction (f_{toward}^{NLO}) is made using $m_b = 4.75$ GeV, a renormalization/factorization scale $\mu = \sqrt{m_b^2 + (p_T^b + p_T^{\bar{b}})/2}$ and CTEQ5M [42] and MRST99 [43] PDFs. To estimate the systematic uncertainty in the NLO calculation, m_b is varied from 4.5–5.0 GeV and μ is varied from 0.5–2.0. To study the effects of large initial state parton transverse momenta (k_T), the NLO prediction is also made with $\langle k_T \rangle$ values of 0–4 GeV. The k_T effects are implemented in the same manner as in ref. [44]. In ref. [44], a $\langle k_T \rangle$ of 3–4 GeV per parton is predicted at the Tevatron. f_{toward}^{NLO} is predicted using MRST99 and CTEQ5M PDFs, respectively, for the different input values of $\langle k_T \rangle$, m_b, and μ. Table V shows the summary of the predictions. The NLO predictions do not depend strongly on the PDF selected. The $f_{forward}^{corr,\mu}$ measured is consistent with the NLO prediction within 1.6 σ for all values of $\langle k_T \rangle$, with the best agreement with $\langle k_T \rangle = 3$ GeV. The $f_{forward}^{corr,e}$ measured differs from the NLO prediction with $\langle k_T \rangle = 4$ GeV at the 3.3 σ level. The measured value is consistent with all $\langle k_T \rangle \leq 3$ GeV at the 1.6 σ level, with the best agreement at $\langle k_T \rangle = 0$ GeV. Since the NLO prediction for $\langle k_T \rangle = 0$ GeV and $\langle k_T \rangle = 3$ GeV differ by only $\sim 2\sigma$ within renormalization/factorization scale uncertainties, it would not be likely to differentiate between scale and k_T effects with a more precise measurement of f_{toward}^{corr}.

Figure 13 illustrate the effects of varying the PDF, $\langle k_T \rangle$, m_b, and renormalization/factorization scale on the NLO predictions in the electron acceptance region. Varying m_b mass does not affect the predicted shape, but instead only affects the total cross section predicted. The two different PDFs studied yields very similar shape and total cross section predictions. Only scale and $\langle k_T \rangle$ variations yield appreciably different shape and to-

	FC	FE	GS	Combined
$f_{toward,mc}^{b\overline{b}\ 90\%}$	$5.1 \pm 0.1\%$	$21.4 \pm 0.5\%$	$46.4 \pm 0.5\%$	$26.4 \pm 0.2\%$
$f_{toward,mc}^{b\to J/\psi X;\overline{b}\to \ell Y}$	$5.8 \pm 0.4\%$	$23.4 \pm 0.8\%$	$47.8 \pm 0.8\%$	$27.3 \pm 0.5\%$
$C_{B\to b}$	0.879 ± 0.063	0.915 ± 0.038	0.971 ± 0.020	0.967 ± 0.019

	FC	FE	GS	Combined
$f_{toward,mc}^{b\overline{b}\ 90\%}$	$3.5 \pm 0.2\%$	$19.5 \pm 0.8\%$	$47.2 \pm 0.8\%$	$25.5 \pm 0.4\%$
$f_{toward,mc}^{b\to J/\psi X;\overline{b}\to \ell Y}$	$3.4 \pm 0.5\%$	$20.4 \pm 1.3\%$	$49.3 \pm 1.2\%$	$26.3 \pm 0.7\%$
$C_{B\to b}$	1.029 ± 0.164	0.956 ± 0.072	0.957 ± 0.028	0.968 ± 0.026

TABLE IV: Correction factor between the experimental measurement and the bottom quarks. Top: Electron sample. Bottom: Muon sample.

NLO MRST99(Electron)	
$\langle k_T \rangle = 0.0$ GeV	$16.9\% \pm 0.2\%$ (stat.)$^{+3.6\%}_{-3.8\%}$ (sys.)
$\langle k_T \rangle = 1.0$ GeV	$19.4\% \pm 0.3\%$ (stat.)$^{+4.8\%}_{-4.1\%}$ (sys.)
$\langle k_T \rangle = 2.0$ GeV	$23.2\% \pm 0.4\%$ (stat.)$^{+5.8\%}_{-5.0\%}$ (sys.)
$\langle k_T \rangle = 3.0$ GeV	$31.9\% \pm 0.6\%$ (stat.)$^{+5.3\%}_{-5.7\%}$ (sys.)
$\langle k_T \rangle = 4.0$ GeV	$44.9\% \pm 0.7\%$ (stat.)$^{+5.4\%}_{-4.8\%}$ (sys.)
NLO CTEQ5M(Electron)	
$\langle k_T \rangle = 0.0$ GeV	$16.5\% \pm 0.2\%$ (stat.)$^{+3.7\%}_{-3.3\%}$ (sys.)
$\langle k_T \rangle = 1.0$ GeV	$19.1\% \pm 0.3\%$ (stat.)$^{+4.9\%}_{-3.9\%}$ (sys.)
$\langle k_T \rangle = 2.0$ GeV	$23.1\% \pm 0.4\%$ (stat.)$^{+5.2\%}_{-5.0\%}$ (sys.)
$\langle k_T \rangle = 3.0$ GeV	$31.7\% \pm 0.6\%$ (stat.)$^{+6.0\%}_{-5.4\%}$ (sys.)
$\langle k_T \rangle = 4.0$ GeV	$45.1\% \pm 0.7\%$ (stat.)$^{+5.5\%}_{-4.6\%}$ (sys.)
PYTHIA(Electron)	$26.4\% \pm 0.2\%$ (stat.)
Data(Electron)	$18.6^{+6.3}_{-5.7}\ ^{+0.5}_{-0.6} \pm 1.7\%$

NLO MRST99(Muon)	
$\langle k_T \rangle = 0.0$ GeV	$16.7\% \pm 0.3\%$ (stat.)$^{+5.2\%}_{-3.6\%}$ (sys.)
$\langle k_T \rangle = 1.0$ GeV	$22.7\% \pm 0.6\%$ (stat.)$^{+6.1\%}_{-7.0\%}$ (sys.)
$\langle k_T \rangle = 2.0$ GeV	$24.7\% \pm 0.6\%$ (stat.)$^{+6.7\%}_{-6.5\%}$ (sys.)
$\langle k_T \rangle = 3.0$ GeV	$32.1\% \pm 0.6\%$ (stat.)$^{+6.4\%}_{-6.9\%}$ (sys.)
$\langle k_T \rangle = 4.0$ GeV	$44.9\% \pm 0.9\%$ (stat.)$^{+5.1\%}_{-6.6\%}$ (sys.)
NLO CTEQ5M(Muon)	
$\langle k_T \rangle = 0.0$ GeV	$16.8\% \pm 0.3\%$ (stat.)$^{+4.1\%}_{-3.8\%}$ (sys.)
$\langle k_T \rangle = 1.0$ GeV	$22.1\% \pm 0.5\%$ (stat.)$^{+5.6\%}_{-5.9\%}$ (sys.)
$\langle k_T \rangle = 2.0$ GeV	$23.8\% \pm 0.9\%$ (stat.)$^{+7.4\%}_{-5.0\%}$ (sys.)
$\langle k_T \rangle = 3.0$ GeV	$31.9\% \pm 0.9\%$ (stat.)$^{+5.7\%}_{-6.5\%}$ (sys.)
$\langle k_T \rangle = 4.0$ GeV	$44.4\% \pm 1.2\%$ (stat.)$^{+7.1\%}_{-5.0\%}$ (sys.)
PYTHIA(Muon)	$25.5\% \pm 0.4\%$ (stat.)
Data(Muon)	$33.4^{+8.9}_{-7.9}\ ^{+7.7}_{-3.0} \pm 2.3\%$

TABLE V: Compilation of the corrected data results, the PYTHIA predictions, and the NLO predictions of f_{toward} Top: Electron. Bottom: Muon.

tal cross section predictions. Varying the renormalization/factorization scale changes the total cross section as expected, lowering the scale increases the total cross section. In addition, the varying the scale changes the prediction rate at large $\Delta\phi^{b\overline{b}}$ (> 2.9 radians) relative to the rest of the distribution, while the shape of < 2.9 radian region varies little. Varying the scale changes the relative rates of $p\overline{p} \to b\overline{b}$ to $p\overline{p} \to b\overline{b}g$ in the NLO prediction. Varying the $\langle k_T \rangle$ on the other hand, changes the predicted $\Delta\phi^{b\overline{b}}$ in a more continuous manner. With the increased number of $J/\psi + \ell$ expected in Run II, a differential azimuthal cross section measurement with 6–12 bins in $\Delta\phi$ should be able to separate scale uncertainty and k_T smearing effects.

V. CONCLUSIONS

APPENDIX A: J/ψ–LEPTON CORRELATION MONTE CARLOS EVENT SAMPLES

Various simulated data set have been necessary for the measurement of f_{toward} in the J/ψ–lepton data sample. The follow section will detail the method of generating the simulated events used in the measurement.

For the bottom impact parameter description, PYTHIA [16, 17] with the CTEQ3L [42] parton distribution functions is used. The bottom quarks are hadronized using the Bowler fragmentation function [45] and using the LUND string fragmentation model. The resulting bottom hadrons are decayed using the CLEO decay model [46]. The events are then placed through a detector simulation [47] and the trigger simulation [48]. The same selection criteria is applied to the J/ψ candidates in Monte Carlos as in data.

For the bottom decay impact parameter shape for muons, the muons are required to be fiducial in both the CMU and the CMP muon subsystems with a SVX track and a $p_T > 3$ GeV.

For the bottom decay shapes for electrons, the electrons are required to be in the CEM fiducial region with

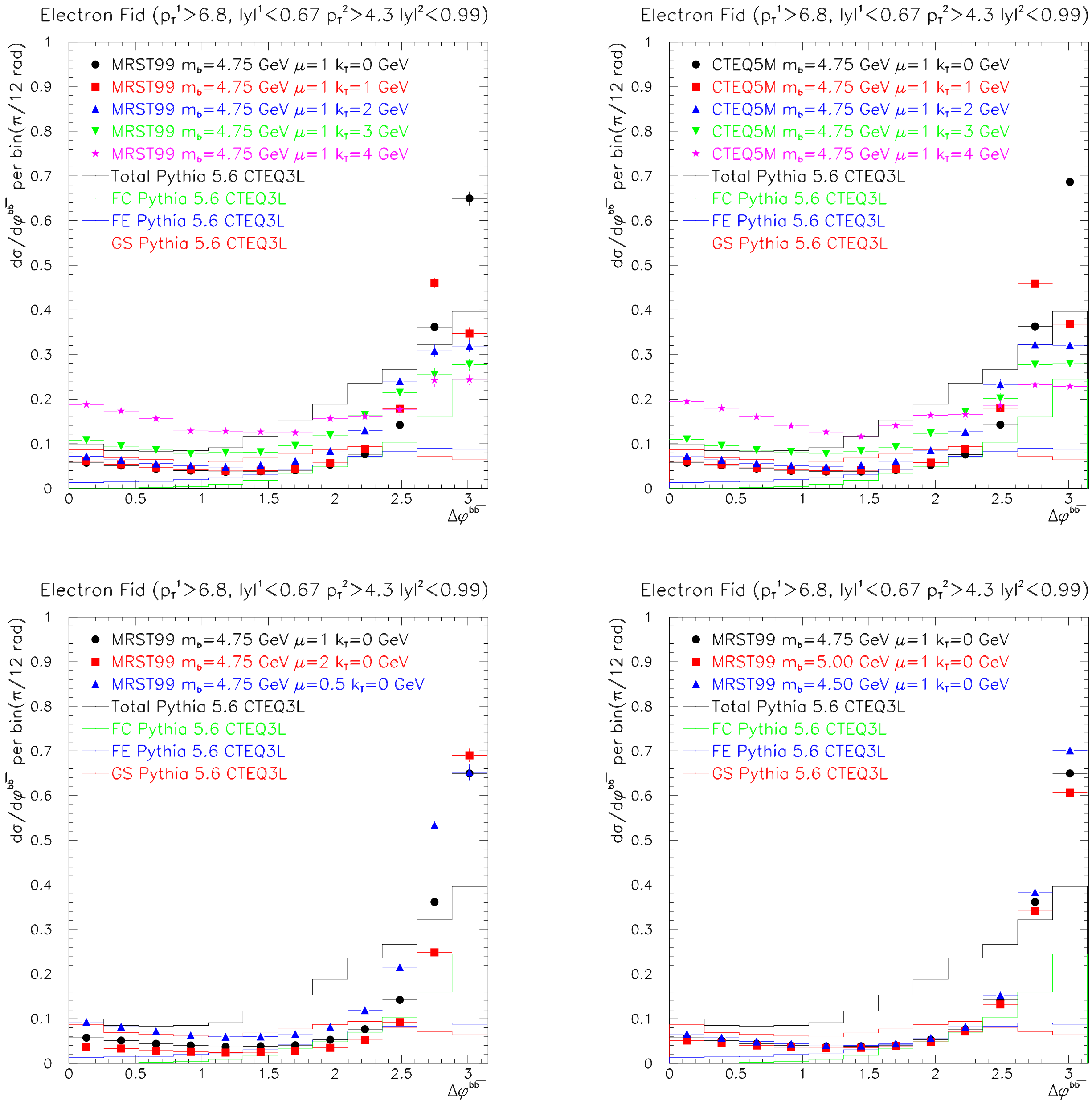

FIG. 13: NLO prediction [1] of bottom spectra in the acceptance region. The PYTHIA prediction is shown as a reference. Top Left: MRST99 PDF varying the additional k_T smearing. Top Right: CTEQ5M PDF varying the additional k_T smearing. Bottom Left: MRST99 PDF varying the renormalization scale μ. Bottom Right: MRST99 PDF varying the bottom quark mass m_B.

a SVX quality track with a $p_T > 2$ GeV. The efficiency of the electron identification criteria is simulated in the same manner as ref. [29]. The CPR, the CES, and the CTC dE/dx selection criteria do not depend on the isolation of the electron, due to the fine segmentation of the CPR, the CES and the CTC. Therefore, the efficiencies as a function of p_T of the CPR and the CES selection derived by ref. [49] using conversions can be used. The CTC dE/dx efficiency as a function of p is defined by the selection criteria. The conversion removal over-efficiency, and the E_{had}/E_{EM} and E/p efficiencies depend on the isolation of the track; therefore, the values simulated in the Monte Carlos have to be used to determine the efficiency.

For residual conversion studies and impact parameter shape determination, the necessary simulated sample was generated in the following manner. A sample of π^0 is simulated in the detector. A SLT conversion candidate is required to have a found track with SVX information in the electron fiducial region with a $p_T > 2$ GeV. The efficiency of electron identification requirements is simulated in the same manner as for the bottom impact parameter shape sample.

The simulated π^0 are generated with a power law spectra for p_T and a flat η distribution. The order of the power law is varied in order to match the p_T spectra of the found SLT conversion candidates in data. The shape of the found pair candidates' p_T is used as a cross check of the power law description of the conversions. Figure 14 shows the Monte Carlo spectra normalized to the data for a power law of 3, 3.5, 4, and 5. The 3.5 order power law describes the data well and is used for the calculation of the efficiency. The 3rd and 4th order power law is used as a estimate of the systematic uncertainty.

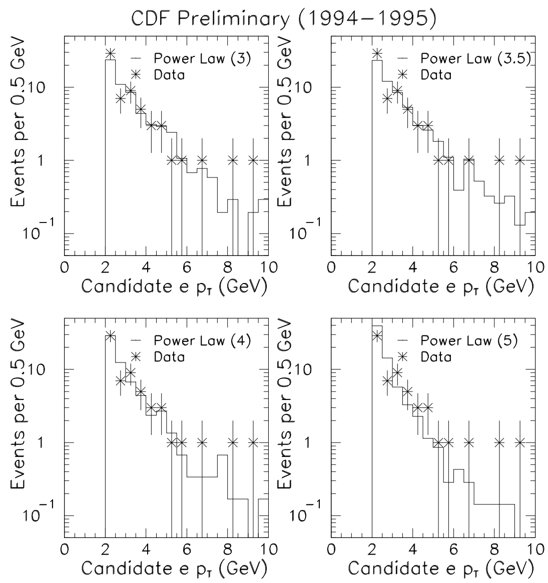

FIG. 14: The p_T spectra of the SLT conversion candidates. Top Left: 3rd order power law. Top Right: 3.5 order power law. Bottom Left: 4th order power law. Bottom Right: 5th order power law.

The p_T of the pair candidates is shown in figure 15. The 3.5 order power law describes the shape of events with $p_T > 0.5$ GeV (where the tracking is assumed to be fully efficient). Half the difference between the 3rd and 4th order power law spectra is used as the systematic uncertainty of the estimate.

The impact parameter–$c\tau$ shape of the B_c background was determined using a Monte Carlos sample. The B_c mesons are generated according to the NLO fragmentation model from ref. [50] with a flat rapidity spectra. The particles are decayed using the semi-leptonic decay model of ref. [51] and passed through a detector and trigger simulation. The selection criteria used is identical to section IV C 2.

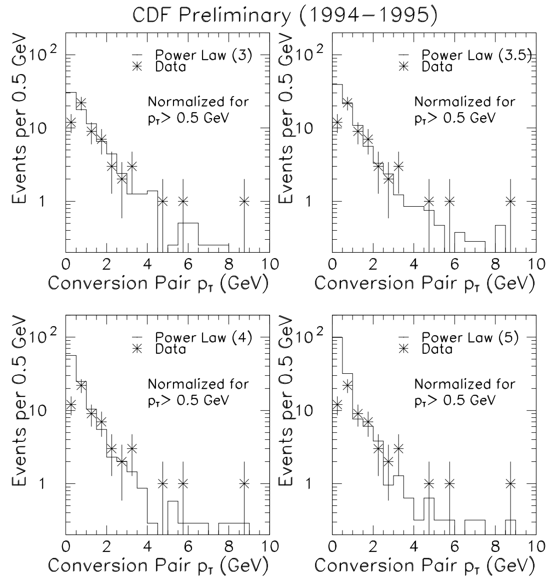

FIG. 15: The p_T spectra of the pair candidates. The Monte Carlos is normalized to the data with $p_T > 0.5$ GeV. Top Left: 3rd order power law. Top Right: 3.5 order power law. Bottom Left: 4th order power law. Bottom Right: 5th order power law.

Single bottom quarks are generated according the next-to-leading order QCD predictions by ref. [52], and fragmented using the Peterson fragmentation model [53]. The resulting bottom hadrons are decayed using the CLEO decay model [46], requiring a $J/\psi \to \mu^+\mu^-$ decay. The events are then placed through a detector simulation [47] and the trigger simulation [48]. For both the calculation of electron and muon fake rates, the J/ψ is required to pass the same selection criteria as data. The sample is normalized to the number of J/ψ events from bottom decay fit in data in section IV C 1.

APPENDIX B: J/ψ–LEPTON CORRELATION LOG-LIKELIHOOD FUNCTION

The fit parameters will be in lower case, the constraints will be upper case, and the errors on the constraints (if applicable) is denoted Δ(Constraint). The superscripts indicate the additional lepton used (e for electrons, μ for muons) and the $\Delta\phi$ region (t for toward, a for away). For example, $N^{e,t}_{B_c}$ is the number of $B_c \to J/\psi e X$ background events estimated in the electron sample in the toward $\Delta\phi$ region.

1. Data

The inputs to the fit on an event-by-event basis are the J/ψ candidate's $c\tau$ and the additional lepton candidate's impact parameter. In the following sections, x with denote the impact parameter, and y will denote the $c\tau$. The number of candidates in the J/ψ mass sideband and signal regions in both $\Delta\phi$ regions is used as a constraint in the likelihood. In the electron sample, the number of found conversions in J/ψ mass sideband and signal regions in both $\Delta\phi$ regions is also used as a constraint. Conversion constraints are discussed later in their respective sections.

$$P(n_{signal}, N_{signal}) = \frac{(n_{signal})^{N_{signal}}}{N_{signal}!} e^{-n_{signal}} \quad \text{(B1)}$$

with the appropriate n_{signal} and N_{signal} for the given sample and $\Delta\phi$ region. n_{signal} is not a fit parameter, but is a function of the other fit parameters, shown in section B 8.

2. $b \to J/\psi X; \bar{b} \to \ell X'$ signal

The shapes which are used for the $b \to J/\psi X; \bar{b} \to \ell X'$ signal are described by the fit functions in sections IV C 1 and IV C 2. The impact parameter and $c\tau$ are assumed to be uncorrelated. Therefore, the shape which describes the signal is the product of the impact parameter shape $(F_b^{d_0}(x))$ and the $c\tau$ shape $(F_b^{c\tau}(y))$ for bottom decay. The parameters that are used in $F_b^{d_0}(x)$ are different for the electron and muon fits.

The number of $b\bar{b}$ events fit is $n_{b\bar{b}}$ with the superscripts given by sample and $\Delta\phi$ region. For example, the number of $b\bar{b}$ events fit in the toward $\Delta\phi$ region in the electron sample is $n_{b\bar{b}}^{e,t}$. The $b\bar{b}$ contribution of the shape component of the likelihood is given by $\frac{n_{b\bar{b}}}{n_{signal}} \cdot F_b^{d_0}(x) \cdot F_b^{c\tau}(y)$ with the appropriate superscripts for the additional lepton type and $\Delta\phi$ region.

3. Unconstrained, uncorrelated backgrounds

The impact parameter–$c\tau$ shapes of the three sources of uncorrelated backgrounds without constraints, considered in this analysis, are constructed using the functions derived in sections IV C 1 and IV C 3. The fit parameters for these three backgrounds are:

- n_{dd}: the number of events with the J/ψ candidate and with the additional lepton candidate both directly produced
- n_{bd}: the number of events with the J/ψ candidate from bottom decay and with the additional lepton candidate produced directly
- n_{db}: the number of events with a directly produced J/ψ candidate and with an additional lepton candidate from bottom decay

where the superscripts indicate of the sample and $\Delta\phi$ region. The number of events with a directly produced J/ψ candidate and an additional lepton candidate from bottom decay is assumed to be small and n_{db} is fixed to zero. The parameter is released and fit for as an estimate of systematic uncertainty due to this assumption.

The shape component of the likelihood for these three backgrounds is assembled in the same manner as the $b\bar{b}$ signal.

4. Residual conversion background

The total number of predicted residual conversions is $R_{conv} \cdot N_{conv}$, where R_{conv} is the ratio between the number of residual versus found conversions and N_{conv} is the number of found conversions in the sample. The number of found conversions removed from the two $\Delta\phi$ regions with the J/ψ candidate in the mass signal region is $N_{conv}^t = 6$ and $N_{conv}^t = 9$, respectively. In section IV C 4, R_{conv} is estimated to be 1.00 ± 0.37, using data and Monte Carlos techniques. Residual conversions are assumed to pair with all three sources of uncorrelated J/ψ candidates: fake J/ψ , directly produced J/ψ, and bottom decay J/ψ. The same value of the fit parameter r_{conv} is used for all sources of J/ψ candidates that pair with the residual conversions. The value of r_{conv} is constrained as a Gaussian probability in the likelihood.

$$G(r_{conv} - R_{conv}, \Delta R_{conv}) = \frac{1}{\sqrt{2}\Delta R_{conv}} e^{-\frac{1}{2}\left(\frac{r_{conv} - R_{conv}}{\Delta R_{conv}}\right)^2} \quad \text{(B2)}$$

The fit parameters that set the scale for the number of residual conversions events with the J/ψ candidate from bottom decay and direct production are n_{bconv} and n_{dconv}. The parameters represent the number of **found** conversions with the J/ψ candidate from the given source. The number of residual conversions fit from these two sources are $r_{conv} \cdot n_{bconv}$ and $r_{conv} \cdot n_{dconv}$. The number of residual conversions already included in the sideband shape component is $r_{side} n_{side}^e f_{conv}^{d_0}$, where $f_{conv}^{d_0} = \frac{r_{conv} \cdot n_{convside}}{N_{sideband}}$ is the fit fraction of J/ψ mass sideband events where the electron is a residual conversion.

Due the relatively small number of residual conversions, fitting all three pairing of J/ψ candidate types with conversions is nit possible. In order to constrain this component of the fit farther, the ratio of between n_{bconv} and n_{dconv} is assumed to be the same as the ratio between J/ψ mesons from bottom decay and J/ψ mesons produced directly (at the primary vertex). The fraction of J/ψ mesons from bottom decay is fit to be $16.6\% \pm 0.2\%$ in section IV C 1, yielding the relationship $n_{bconv}^{t/a} = 0.2 \cdot n_{dconv}^{t/a}$. As an estimate of the systematic uncertainty, $n_{bconv}^{t/a}$ and $n_{dconv}^{t/a}$ are fixed to zero in separate fits in order to probe the full range of ratio $n_{bconv}^{t/a} : n_{dconv}^{t/a}$.

The number of found conversions in the two $\Delta\phi$ regions is used as a constraint on the fit of the residual conversions. The number of 'found' conversions fit is the number of residual conversions fit divided by the ratio of residual versus found conversions:

$$n_{conv} \equiv n_{bconv} + n_{dconv} + \frac{r_{side} n_{side}^{e} n_{convside}}{N_{sideband}} \tag{B3}$$

The constraint using the number of found conversions is the Poisson probability of finding N_{conv} conversion candidates with a mean value of number of found conversion fit.

$$P(n_{conv}, N_{conv}) = \frac{(n_{conv})^{N_{conv}}}{N_{conv}!} e^{-(n_{conv})} \tag{B4}$$

5. Fake J/ψ backgrounds

The fake J/ψ impact parameter–$c\tau$ background shape ($F_{sideband}^{\mu}$) is determined in section IV C 6 from a fit to the data for the muon sample. The predicted number of events for this background is the ratio between the number of fake J/ψ events in the J/ψ mass signal and sideband region (R_{side}) times the number of events seen in data with the J/ψ candidate in the mass sideband regions (N_{side}) for the given sample and $\Delta\phi$ region.

In section IV B, the ratio is determined to be $R_{side} = 0.501 \pm 0.044$ from a fit of the total J/ψ data sample. The same value for the fit parameter r_{side} is used in both $\Delta\phi$ regions in the sample, but can be different in the electron and muon samples. The fit value of r_{side} is constrained using a Gaussian factor in the likelihood function.

$$G(r_{side} - R_{side}, \Delta R_{side}) = \frac{1}{\sqrt{2}\Delta R_{side}} e^{-\frac{1}{2}\left(\frac{r_{side}-R_{side}}{\Delta R_{side}}\right)^2} \tag{B5}$$

The corresponding fit parameter n_{side}, for the given sample and $\Delta\phi$ region, is constrained using the Poisson probability of measuring N_{side} events for a sample with an average of n_{side} events.

$$P(n_{side}, N_{side}) = \frac{(n_{side})^{N_{side}}}{N_{side}!} e^{-n_{side}} \tag{B6}$$

The contribution of the shape component of the likelihood is $\frac{r_{side} n_{side}}{n_{signal}} \cdot F_{side}(x, y)$ for the given sample and $\Delta\phi$ region.

The fake J/ψ background component in the electron sample is treated differently due to the presence of residual conversions in the background. The fake J/ψ shape is fit at the same time as the J/ψ signal region. The f_{conv} component of the fake J/ψ impact parameter–$c\tau$ shape is a composite of two variables which are constrained. $f_{conv} = \frac{r_{conv} \cdot n_{convside}}{N_{sideband}}$ where r_{conv}, $n_{convside}$, and $N_{sideband}$ are the fit ratio of residual to found conversion, fit number of "found" conversions, and $N_{sideband} = N_{side}^{e,t} + N_{side}^{\mu,a}$. $n_{convside}$ is constrained by the number of conversions found in the sideband using the Poisson probability:

$$P(n_{convside}, N_{convside}) = \frac{(n_{convside})^{N_{convside}}}{N_{convside}!} e^{-n_{convside}} \tag{B7}$$

6. $B_c \to J/\psi \ell X$ backgrounds

$B_c \to J/\psi \ell X$ background is predicted to only populate the toward region in $\Delta\phi$. The expected number of B_c events is constrained in the likelihood as a Gaussian probability factor.

$$G(n_{B_c} - N_{B_c}, \Delta N_{B_c}) = \frac{1}{\sqrt{2}\Delta N_{B_c}} e^{-\frac{1}{2}\left(\frac{n_{B_c}-N_{B_c}}{\Delta N_{B_c}}\right)^2} \tag{B8}$$

where ΔN_{B_c} is the positive-sided error of N_{B_c} if $(n_{B_c} - N_{B_c}) \geq 0.0$, and the negative-sided error otherwise.

7. $b \to J/\psi \ell_{fake} X$ backgrounds

As in the B_c background, $b \to J/\psi \ell_{fake} X$ background events are only expected to populate the toward region in $\Delta\phi$, and therefore the background is only fit for in the toward region in the two samples. The expected number is $b \to J/\psi \ell_{fake} X$ events is used as a constraint to the likelihood in the same way as B_c.

$$G(n_{B_{fake}} - N_{B_{fake}}, \Delta N_{B_{fake}}) = \frac{1}{\sqrt{2}\Delta N_{B_{fake}}} \times e^{-\frac{1}{2}\left(\frac{n_{B_{fake}}-N_{B_{fake}}}{\Delta N_{B_{fake}}}\right)^2}$$

8. n_{signal} sums

The number of events fit in the J/ψ mass signal region is a function of fit parameters described previously in this section. Listed below are the functions for number of events fit for the two samples and $\Delta\phi$ regions.

$$n_{signal}^{\mu,t} = n_{b\bar{b}}^{\mu,t} + n_{bd}^{\mu,t} + n_{db}^{\mu,t} + n_{dd}^{\mu,t} + r_{side}^{\mu} \cdot n_{side}^{\mu,t} + n_{B_c}^{\mu,t} + n_{B_{fake}}^{\mu,t} \tag{B9}$$

$$n^{\mu,a}_{signal} = n^{\mu,a}_{b\bar{b}} + n^{\mu,a}_{bd} + n^{\mu,a}_{db} + n^{\mu,a}_{dd} + r^{\mu}_{side} \cdot n^{\mu,a}_{side} \tag{B10}$$

$$n^{e,t}_{signal} = n^{e,t}_{b\bar{b}} + n^{e,t}_{bd} + n^{e,t}_{db} + n^{e,t}_{dd} + r^{e}_{side} \cdot n^{e,t}_{side} + n^{e,t}_{B_c} + n^{e,t}_{B_{fake}} + r_{conv} \cdot n^{t}_{bconv} + r_{conv} \cdot n^{t}_{dconv} \tag{B11}$$

$$n^{e,a}_{signal} = n^{e,a}_{b\bar{b}} + n^{e,a}_{bd} + n^{e,a}_{db} + n^{e,a}_{dd} + r^{e}_{side} \cdot n^{e,a}_{side} + r_{conv} \cdot n^{t}_{bconv} + r_{conv} \cdot n^{t}_{dconv} \tag{B12}$$

9. Impact parameter–$c\tau$ shape component

The complete functions for the shape components of the fit are given below for the two samples and $\Delta\phi$ regions. As a reminder, x is the additional lepton candidate's impact parameter and y is the J/ψ candidate's $c\tau$.

$$F^{\mu,t}_{shape}(x,y) = \frac{1}{n^{\mu,t}_{signal}}\Big[n^{\mu,t}_{b\bar{b}} F^{c\tau,\mu}_{b}(y) F^{d_0,\mu}_{b}(x) + n^{\mu,t}_{bd} F^{c\tau,\mu}_{b}(y) F^{d_0,\mu}_{direct}(x) + n^{\mu,t}_{db} F^{c\tau,\mu}_{direct}(y) F^{d_0,\mu}_{b}(x) \tag{B13}$$

$$+ n^{\mu,t}_{dd} F^{c\tau,\mu}_{direct}(y) F^{d_0,\mu}_{direct}(x) + n^{\mu,t}_{B_{fake}} F^{\mu}_{B_{fake}}(x,y) + n^{\mu,t}_{B_c} F^{\mu}_{B_c}(x,y) + r^{\mu}_{side} n^{\mu,t}_{side} F^{\mu}_{side}(x,y)\Big] \tag{B14}$$

$$F^{\mu,a}_{shape}(x,y) = \frac{1}{n^{\mu,a}_{signal}}\Big[n^{\mu,a}_{b\bar{b}} F^{c\tau,\mu}_{b}(y) F^{d_0,\mu}_{b}(x) + n^{\mu,a}_{bd} F^{c\tau,\mu}_{b}(y) F^{d_0,\mu}_{direct}(x) + n^{\mu,a}_{db} F^{c\tau,\mu}_{direct}(y) F^{d_0,\mu}_{b}(x) \tag{B15}$$

$$+ n^{\mu,a}_{dd} F^{c\tau,\mu}_{direct}(y) F^{d_0,\mu}_{direct}(x) + r^{\mu}_{side} n^{\mu,a}_{side} F^{\mu}_{side}(x,y)\Big] \tag{B16}$$

$$F^{e,t}_{shape}(x,y) = \frac{1}{n^{e,t}_{signal}}\Big[n^{e,t}_{b\bar{b}} F^{c\tau,e}_{b}(y) F^{d_0,e}_{b}(x) + n^{e,t}_{bd} F^{c\tau,e}_{b}(y) F^{d_0,e}_{direct}(x) + n^{e,t}_{db} F^{c\tau,e}_{direct}(y) F^{d_0,e}_{b}(x) \tag{B17}$$

$$+ n^{e,t}_{dd} F^{c\tau,e}_{direct}(y) F^{d_0,e}_{direct}(x) + n^{e,t}_{B_{fake}} F^{e}_{B_{fake}}(x,y) + n^{e,t}_{B_c} F^{e}_{B_c}(x,y) \tag{B18}$$

$$+ r^{e}_{side} n^{e,t}_{side} F^{e}_{side}(x,y) + r_{conv} n^{t}_{bconv} F_{conv}(x) F^{c\tau,e}_{b}(y) + r_{conv} n^{t}_{dconv} F_{conv}(x) F^{c\tau,e}_{direct}(y)\Big] \tag{B19}$$

$$F^{e,a}_{shape}(x,y) = \frac{1}{n^{e,a}_{signal}}\Big[n^{e,a}_{b\bar{b}} F^{c\tau,e}_{b}(y) F^{d_0,e}_{b}(x) + n^{e,a}_{bd} F^{c\tau,e}_{b}(y) F^{d_0,e}_{direct}(x) + n^{e,a}_{db} F^{c\tau,e}_{direct}(y) F^{d_0,e}_{b}(x) \tag{B20}$$

$$+ n^{e,a}_{dd} F^{c\tau,e}_{direct}(y) F^{d_0,e}_{direct}(x) + r^{e}_{side} n^{e,a}_{side} F^{e}_{side}(x,y) + r_{conv} n^{a}_{bconv} F_{conv}(x) F^{c\tau,e}_{b}(y) \tag{B21}$$

$$+ r_{conv} n^{a}_{dconv} F_{conv}(x) F^{c\tau,e}_{direct}(y)\Big] \tag{B22}$$

10. Bin constraints component

The constraints which are specific to a given region in $\Delta\phi$ and sample are listed below:

$$C^{\mu,t}_{bin} = P(n^{\mu,t}_{signal}, N^{\mu,t}_{signal}) \cdot P(n^{\mu,t}_{side}, N^{\mu,t}_{side}) \cdot G(n^{\mu,t}_{B_c} - N^{\mu,t}_{B_c}, \Delta N^{\mu,t}_{B_c}) \cdot G(n^{\mu,t}_{B_{fake}} - N^{\mu,t}_{B_{fake}}, \Delta N^{\mu,t}_{B_{fake}}) \tag{B23}$$

$$C^{\mu,a}_{bin} = P(n^{\mu,a}_{signal}, N^{\mu,a}_{signal}) \cdot P(n^{\mu,a}_{side}, N^{\mu,a}_{side}) \tag{B24}$$

$$C^{e,t}_{bin} = P(n^{e,t}_{signal}, N^{e,t}_{signal}) \cdot P(n^{e,t}_{side}, N^{e,t}_{side}) \cdot G(n^{e,t}_{B_c} - N^{e,t}_{B_c}, \Delta N^{e,t}_{B_c}) \tag{B25}$$

$$\times\ G(n^{e,t}_{B_{fake}} - N^{e,t}_{B_{fake}}, \Delta N^{e,t}_{B_{fake}}) \cdot P(n^{t}_{conv}, N^{t}_{conv}) \tag{B26}$$

$$C^{e,a}_{bin} = P(n^{e,a}_{signal}, N^{e,a}_{signal}) \cdot P(n^{e,a}_{side}, N^{e,a}_{side}) \cdot P(n^{a}_{conv}, N^{a}_{conv}) \tag{B27}$$
$$\tag{B28}$$

11. Global constraints component

The global constraints are the simplest component of the likelihood. The functions of the global constraints are listed below:

$$C^{\mu}_{global} = G(r^{\mu}_{side} - R_{side}, \Delta R_{side}) \tag{B29}$$
$$C^{e}_{global} = G(r^{e}_{side} - R_{side}, \Delta R_{side}) \tag{B30}$$
$$\times\ G(r_{conv} - R_{conv}, \Delta R_{conv}) \tag{B31}$$

12. Log-likelihood function

Finally, the log-likelihood can be assembled from the functions developed in the previous sections. The likelihood function for the muon sample is:

$$\mathcal{L} = C^{\mu}_{global} \prod_{i}^{t,a} \left[C^{\mu,i}_{bin} \prod_{j}^{N^{\mu,i}_{signal}} \left(F^{\mu,i}_{shape}(x^{\mu}_{i,j}, y^{\mu}_{i,j}) \right) \right]$$

where $x^{\mu}_{i,j}$ and $y^{\mu}_{i,j}$ are the impact parameter of the additional muon candidate and the $c\tau$ of the J/ψ candidate for j^{th} event in the i^{th} $\Delta\phi$ region in the J/ψ signal region.

The likelihood function for the electron sample is similar to the muon likelihood. The electron likelihood includes conversion terms and the fit of the J/ψ mass sideband region.

$$\mathcal{L} = C^{e}_{global} \prod_{i}^{t,a} \left[C^{e,i}_{bin} \prod_{j}^{N^{e,i}_{signal}} \left(F^{e,i}_{shape}(x^{e}_{i,j}, y^{e}_{i,j}) \right) \right]$$
$$\times\ P(n_{convside}, N_{convside}) \cdot \prod_{k}^{N_{sideband}} (F_{conv}(x^{e}_{k}, y^{e}_{k}))$$

where $x^{e}_{i,j}$ and $y^{e}_{i,j}$ are the impact parameter of the additional electron candidate and the $c\tau$ of the J/ψ candidate for j^{th} event in the i^{th} $\Delta\phi$ region in the J/ψ signal region, and x^{e}_{k} and y^{e}_{k} are the impact parameter of the additional electron candidate and the $c\tau$ of the J/ψ candidate for k^{th} event in the J/ψ sideband region.

APPENDIX C: TESTS OF J/ψ–LEPTON CORRELATION LOG-LIKELIHOOD FIT

The impact parameter–$c\tau$ likelihood is tested using a large set of toy Monte Carlo samples. First, the inputed means for the various fit components are chosen to be similar to the results in data. The constrained terms are chosen to be consistent with the constraint. These inputs are Poisson fluctuated to determine the composition of each sample. Each 'event' is assigned an impact parameter and $c\tau$ according to the shape function used to describe that type of event .

Next, the fit constraints not yet varied (R_{side}, R_{conv}, $N_{B_{fake}}$, N_{B_c}, N^{t}_{conv}, N^{a}_{conv}, and $N_{convside}$) are fluctuated using the appropriate statistic. The fluctuated constraints are then used in the fit of the toy Monte Carlos sample.

A total of 1000 samples are generated and fit for both the electron and muon samples. The fit values are not forced to be non-negative. The pull is calculated for each fit value relative to the non-fluctuated input quantities. The pull is equal to width of the $\frac{n-\mu}{\sigma_n}$ distribution where n is the fit value, σ_n is the fit error returned, and μ is the average value of the parameter input. The bias, which is the mean of the $\frac{n-\mu}{\sigma_n}$ distribution, is also measured. Finally, the average difference between the fitted value and input parameter is calculated, $\overline{(x - \overline{x})}$.

The pulls, biases, and average differences for all variables are acceptable for both test samples. All pulls are within $\pm 6\%$ of 1 and all biases are within $\pm 0.12\sigma$ of 0. Allowing the likelihood to have negative components yields fit results with meaningful fit values and errors.

Figure 16 shows the minimum log-likelihood distributions of both samples. 19.6% of the muon toy Monte Carlos samples and 49.8% of the electron toy Monte Carlos samples have a higher minimum log-likelihood than the data. The minimum log-likelihood distributions along with the biases, pulls, and average differences give confidence that the likelihood is working properly and describes the data.

The muon toy Monte Carlos samples has an input mean of $f^{input}_{towards} = 34.5\%$ and fit a mean of $f^{fit}_{towards} = 34.5 \pm 0.4\%$. The width of the fit $f_{towards}$ distribution is $10.9 \pm 0.3\%$ which is consistent with the error seen in data of $^{+9.2}_{-8.2}\%$. The electron toy Monte Carlos have a mean of $f^{fit}_{towards} = 18.6 \pm 0.2\%$ with a width of 6.0 ± 0.1. The input value is $f^{input}_{towards} = 19.2\%$ and the fit error of $^{+6.5}_{-5.8}\%$, both which are consistent with the fit values.

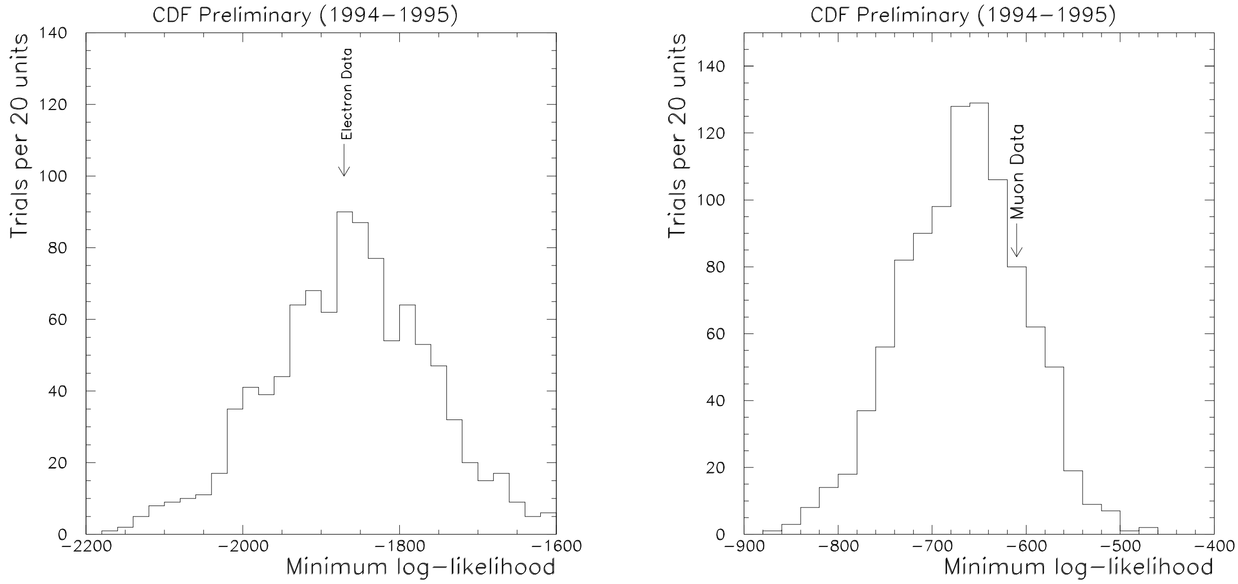

FIG. 16: The minimum log-likelihood distributions of the toy Monte Carlos Left: Electrons Right: Muons.

[1] P. N. M. Mangano and G. Ridolfi, Nucl. Phys. B **373**, 292 (1992).
[2] C. Albajar et al., Phys. Lett. B **256**, 121 (1991).
[3] F. Abe et al., Phys. Rev. Lett. **71**, 50 (1993).
[4] F. Abe et al., Phys. Rev. Lett. **71**, 2396 (1993).
[5] F. Abe et al., Phys. Rev. Lett. **75**, 1451 (1995).
[6] D. Acosta et al., Phys. Rev. D **65**, 052005 (2002).
[7] S. Abachi et al., Phys. Rev. Lett. **74**, 2632 (1995).
[8] B. Abbott et al., Phys. Rev. Lett. **85**, 5068 (2000).
[9] C. Albaja et al., Z. Phys. C **61**, 41 (1994).
[10] B. Abbott et al., Phys. Lett. B **487**, 264 (2000).
[11] F. Abe et al., Phys. Rev. D **53**, 1051 (1996).
[12] F. Abe et al., Phys. Rev. D **55**, 2546 (1997).
[13] E. L. Berger et al., Phys. Rev. Lett. **86**, 2001 (2001).
[14] M. Cacciari and P. Nason, Phys. Rev. Lett. **89**, 122003 (2002).
[15] W. Y. K. F. Halzen and D. M. Scott, Phys. Rev. D **27**, 1631 (1983).
[16] T. Sjostrand and M. Bengtson, Comput. Phys. Comm. **43**, 367 (1987).
[17] H.-U. Bengtsson and T. Sjostrand, Comput. Phys. Comm. **46**, 43 (1987).
[18] G. Marchesini et al., Comput. Phys. Comm. **67**, 465 (1992).
[19] R. D. Field, Phys. Rev. D **65**, 094006 (2002).
[20] F. Abe et al., Nucl. Instrum. Methods A **271**, 387 (1988).
[21] F. Bedeschi et al., Nucl. Instrum. Methods A **271**, 387 (1995).
[22] P. Azzi et al., Nucl. Instrum. Methods A **360**, 137 (1995).
[23] L. Balka et al., Nucl. Instrum. Methods A **267**, 272 (1988).
[24] S. Bertolucci et al., Nucl. Instrum. Methods A **267**, 301 (1988).
[25] G. Ascoli et al., Nucl. Instrum. Methods A **268**, 33 (1988).
[26] J. D. Lewis et al., CDF public note 2858, CDF (1994).
[27] F. Abe et al., Phys. Rev. D **60**, 072003 (1999).
[28] J. Heinrich et al., CDF internal note 4745, CDF (1998).
[29] F. Abe et al., Phys. Rev. D **58**, 112004 (1998).
[30] A. Bardi et al., Nucl. Instrum. Methods A **485**, 178 (2002).
[31] J. Marriner, CDF public note 1996, CDF (1993).
[32] F. Abe et al., Phys. Rev. D **57**, 538 (1998).
[33] F. Abe et al., Phys. Rev. Lett. **85**, 2886 (2000).
[34] D. E. Groom et al., Eur. Phys. J. C **15**, 1 (2000).
[35] F. Abe et al., Phys. Rev. D **61**, 072005 (2000).
[36] O. Long et al., CDF internal note 4315, CDF (1997).
[37] J. Suzuki, Ph.D. thesis, University of Tsukuba (1998).
[38] F. James and M. Roos, Comput. Phys. Comm. **10**, 343 (1975).
[39] P. Sphicas, CDF internal note 2655, CDF (1994).
[40] K. Hagiwara et al., Phys. Rev. D **66**, 010001 (2002).
[41] F. Abe et al., Phys. Rev. D **61**, 032001 (2000).
[42] H. L. Lai et al., Phys. Rev. D **51**, 4763 (1995).
[43] A. D. Martin et al., Eur. Phys. J. C **4**, 463 (1999).
[44] L. Apanasevich et al., Phys. Rev. D **59**, 074007 (1999).
[45] M. G. Bowler, Z. Phys. C **11**, 169 (1981).
[46] P. Avery et al., Cornell Internal Note CSN-112, CLEO (1985).
[47] M. Shapiro et al., CDF Public Note 1810, CDF (1992).
[48] S. Pappas, CDF internal note 3537, CDF (1996).
[49] C. Campagnari and D. Kestenbaum, CDF internal note 3682, CDF (1996).
[50] E. Braaten et al., Phys. Rev. D **48**, 5049 (1993).
[51] N. Isgur et al., Phys. Rev. D **39**, 2002 (1998).
[52] P. Nason et al., Nucl. Phys. B **327**, 49 (1989).

[53] C. Peterson et al., Phys. Rev. D **27**, 105 (1983).